The Canadian MC2: A Semi-Lagrangian, Semi-Implicit Wideband Atmospheric Model Suited for Finescale Process Studies and Simulation

ROBERT BENOIT, MICHEL DESGAGNÉ, PIERRE PELLERIN, SIMON PELLERIN, AND YVES CHARTIER

Recherche en Prévision Numérique, Environment Canada, Dorval, Québec, Canada

SERGE DESJARDINS

Maritime Weather Centre, Environment Canada, Bedford, Nova Scotia, Canada

(Manuscript received 14 October 1996, in final form 3 February 1997)

ABSTRACT

This paper attempts to document the developmental research and early mesoscale results of the new fully nonhydrostatic atmospheric model called MC2 (mesoscale compressible community). Its numerical scheme is the semi-implicit semi-Lagrangian approach conceived and demonstrated by Tanguay, Robert, and Laprise. The dominant effort required to become a full-fledged mesoscale model was to connect it properly to a full-scale and evolving physics package; the enlarged scope of a package previously dedicated to hydrostatic pressure coordinate-type models posed some new questions. The one-way nesting is reviewed and particularly the self-nesting or cascade mode; the potential implication of this mode is explored with a stand-alone forecast experiment and related to the other existing approach employing hemispheric or global variable meshes. One of the strong assets of MC2 is its growing community of users and developers. To demonstrate the wideband characteristic of MC2, that is, its applicability to a large range of atmospheric flows, two very different cases are studied: an Atlantic winter East Coast cyclogenesis (meso-α scale, mostly hydrostatic) and a local (meso-γ scale, partly nonhydrostatic) downslope windstorm occuring over unexpectedly modest topography (Cape Breton Highlands of Nova Scotia, Canada).

1. Introduction

Progress in the quality of atmospheric modeling of significant weather events results from advancement in the use of more accurate sets of governing equations (both the continuous forms and the numerical discretization), as well as from more precise observations to define the boundary conditions for the models.

About 20 years ago, Tapp and White (1976) pioneered a category of implicit methods, which is one way to reconcile higher accuracy of model equations with the long time steps suitable for mesoscale model integrations. The other main avenue toward efficient nonhydrostatic models was that of Klemp and Wilhelmson (1978), who used time splitting with a semi-implicit scheme to handle the acoustic waves but remained explicit for all other wave types. Tanguay et al. (1990, TRL hereafter) have demonstrated the feasibility and efficiency of NWP integrations based on a nonhydrostatic model governed by the fully compressible Euler equations, also called the Navier–Stokes equations. The Euler equations include the full time derivatives of all three components of velocity as well as the complete continuity equation. Therefore they are applicable to the simulation of an extremely wide spectrum of atmospheric motions. In view of the large disparity—two to three orders of magnitude—between the 1-s time step needed with an explicit scheme for the vertically propagating acoustic waves in a 350-m vertical mesh size and the $O(1000)$-s time step used by current operational NWP hydrostatic models having a similar vertical resolution, it is obvious that TRL's major contribution is the efficiency of the numerical scheme that they developed in order to solve the compressible governing equations.

The MC2 (mesoscale compressible community) model is the ultimate model inherited from Robert before his death in November 1993; it is probably the only currently available 3D fully compressible model that uses a semi-implicit semi-Lagrangian (SISL) time scheme.

Starting with the fully elastic nonhydrostatic model developed by TRL, a group of scientists from Recherche en Prévision Numérique (RPN) and Université du Québec à Montréal (UQAM) has worked actively since May 1992 to provide this versatile modeling tool, applicable to a variety of needs of the atmospheric–hydrologic research community in Canada and abroad.

Corresponding author address: Dr. Robert Benoit, 5th Floor, 2121 Transcanada Road, Suite 564, Dorval, QC H9P 1J3 Canada.
E-mail: Robert.Benoit@ec.gc.ca

The team's commitment has been to adapt the model coding to current RPN standards, to provide extensive documentation, to include all necessary features (such as nesting, boundary layer, convection, radiation) needed for the known current applications, and to maintain a central model library (with contributed modules from the community) that allows easy porting to various computers. By January 1994, the objective was reached and the delivery of the model to research groups was started. The MC2 community soon became international. Support to remote users as well as contributions to the central community model library now take place.

This historical path is similar to that of the National Center for Atmospheric Research (NCAR) series of MM*x* models, particularly the MM5 (Grell et al. 1993). Both nonhydrostatic models (MM5 and MC2) became available at about the same time. The development of MM5 took place over about 15 years if we trace it back to Anthes and Warner (1978), while that of MC2 occured over just 8 years, starting with the SISL LAM (limited-area model) of Robert and Yakimiw (1986). Correspondingly, the user community of the MM5 model is much larger, with over 200 users in 50 institutions, compared to 50 users located in about 20 institutions for MC2. In each case, the community is supported at the central site by the equivalent of one full-time person and training classes are offered. As will be seen below in section 2, the key feature of MC2 is a more modern [but perhaps less efficient; see Bartello and Thomas (1996)] unified treatment—the SISL scheme—of the compressible dynamics. Another widespread model that now has a nonhydrostatic option is the Colorado State University RAMS (Pielke et al. 1992).

RPN's main mandate is to deliver new or improved NWP models to the Canadian Meteorological Centre (CMC). In the trend set up by the Regional Finite Element (RFE) model (Mailhot et al. 1995a), an ambitious objective was defined in 1990 to develop a global variable mesh finite-element model, called GEF (Côté et al. 1993; Côté et al. 1995). The aim is to replace both operational regional RFE and global spectral (Ritchie 1991) models by a unique one, GEF, that can be applied both on a uniform mesh (for global forecasts and data assimilation) and on a focused, but still global, mesh for regional products. Since the trend of the regional models in different countries is toward higher and higher resolution of mesoscale phenomena, the set of governing equations for the GEF model will eventually have to be changed to the compressible equations. Later, the MC2 project started in 1992 at RPN and offered the possibility to experiment almost immediately with NWP problems related to nonhydrostatic effects. Other effects devolved from the MC2 project are a rapid advance in the improved coupling of physics to nonhydrostatic models and the evaluation of the limited-area approach for the mesoscale forecasting.

At this stage with MC2, it has not yet been possible to include any improvement in the observational content of the initial or boundary conditions, which is surely the next most serious barrier to be addressed in future mesoscale modeling research. The small-scale results to be reported here relate to the class of mesoscale phenomena that are strongly *forced by the surface* conditions such as terrain/coastline, etc. The reader will see that very detailed topography is inserted in some of the runs presented: at this point, this is the only smaller-scale data injected in the model. In that sense, our demonstration of the performance of MC2 is restricted at the present and will only become applicable to all classes of mesoscale phenomena when we do a proper mesoscale data assimilation for initial and boundary conditions—the key to forecasting *transient* processes such as squall lines, rainbands, etc.

The *current* knowledge of the advantage of the semi-Lagrangian (SL) method over the Eulerian method for meso-β-/γ-scale models is not presented here. Pellerin et al. (1995) examined the advection–condensation problem, one of the dominant physical processes in this category of models. By comparing simulations of a moist buoyant bubble, they concluded that the noise level of an SL model is less severe, allows larger time steps, and that ''a given level of accuracy can be obtained with coarser resolution'' (Pellerin et al. 1995, 3329).

The plan of this paper is quite simple. Apart from reviewing MC2's formulation (section 2), we present our work on the interfacing of a preexisting physics package, with emphasis on the change in vertical coordinate and discretization, and consideration to lateral nesting for the forcings (section 3). Next (section 4) the treatment of the nesting is covered, both for the lateral and upper boundaries. Initialization is documented and we distinguish between two possible modes of using the model, simulation and forecast; an example is given. Following that, in section 5, are the results, showing the performance of MC2 in both present and future types of environment for mesoscale NWP models: one ''hydrostatic'' problem at meso-α scale and another flow problem at the meso-γ scale where the ''nonhydrostatic'' component is important. In this manner, we complete a clean demonstration of the advantage of more accurate governing equations. The summary is in section 6.

2. The nonhydrostatic model

A detailed description of the dynamical equations of MC2 is made by Laprise (1995) and a discussion of the principal features of the numerical response, particularly for the SISL handling of the gravity waves, is presented elsewhere (Pinty et al. 1995).

We give a brief summary of Robert's formulation of the MC2 model. The Euler equations for a gas on a sphere with no topography, once projected to conformal coordinates X and Y, take the form

$$\frac{dU}{dt} = fV - K\frac{\partial S}{\partial X} - RT\frac{\partial q}{\partial X} + F_U, \quad (2.1)$$

$$\frac{dV}{dt} = -fU - K\frac{\partial S}{\partial Y} - RT\frac{\partial q}{\partial Y} + F_V, \quad (2.2)$$

$$\delta_h\frac{dw}{dt} = -g - RT\frac{\partial q}{\partial z} + F_w, \quad (2.3)$$

$$(1 - \alpha)\frac{dq}{dt} = -S\left(\frac{\partial U}{\partial X} + \frac{\partial V}{\partial Y}\right) - \frac{\partial w}{\partial z} + \frac{F_T}{T}, \quad (2.4)$$

$$\frac{dT}{dt} = \alpha T\frac{dq}{dt} + F_T, \quad (2.5)$$

$$\frac{dM}{dt} = F_M, \quad (2.6)$$

$$\frac{dC}{dt} = F_C. \quad (2.7)$$

The symbols have their usual meaning or have been defined in TRL. We recall that $q = \log(p/p_0)$, with p_0 a constant, $\alpha = R/C_p$. Equation (2.4) is the pressure equation, resulting from the combination of the continuity and thermodynamic equations. A switch, δ_h, is introduced in (2.3) to allow running the model in hydrostatic mode. The various F_i's are the eddy forcing terms due to the subgrid-scale physical processes, described below. Note that so far we used $F_w = 0$ and that the F_T/T term of (2.4) is not included. The last two equations [(2.6) and (2.7)] are pure scalar advections for the specific densities of water substance (M, vapor; C, condensed water) that decouple from the MC2 dynamics.

At this point, the total derivative

$$\frac{d}{dt} = \frac{\partial}{\partial t} + S\left(U\frac{\partial}{\partial X} + V\frac{\partial}{\partial Y}\right) + w\frac{\partial}{\partial z} \quad (2.8)$$

is expressed in terms of the horizontal wind images,

$$\begin{pmatrix} U \\ V \end{pmatrix} = \frac{1}{m}\begin{pmatrix} -\sin\lambda & -\cos\lambda \\ \cos\lambda & -\sin\lambda \end{pmatrix}\begin{pmatrix} u \\ v \end{pmatrix}, \quad (2.9)$$

and the geometric vertical component $w = dz/dt$. Here S is the square of the map scale factor m and the conformal projection is usually chosen to be the conventional polar stereographic. The Mercator projection is currently being implemented in the model file environment for improved simulation over equatorial latitudes.

The orography is introduced in the model following Gal-Chen and Somerville (1975), using the Gal-Chen height coordinate

$$\zeta(X, Y, z) = \left[\frac{z - h_0(X, Y)}{H - h_0(X, Y)}\right]H, \quad (2.10)$$

with H being the top of the model atmosphere and $h_0(X, Y)$ the topographic height. Note that ζ is terrain following and vertical, that is, not orthogonal to the surface. To allow variable vertical resolution, a mapping of ζ, $Z(\zeta)$, is introduced and the discrete form of the metric coefficient $\partial\zeta/\partial Z$ is used throughout the model dynamics. The vertical discrete levels can thus remain uniformly spaced in Z, the generalized Gal-Chen coordinate.

The inclusion of topography modifies the expression for the total derivative (2.8),

$$\frac{d}{dt} = \left(\frac{\partial}{\partial t}\right)_Z + S\left[U\left(\frac{\partial}{\partial X}\right)_Z + V\left(\frac{\partial}{\partial Y}\right)_Z\right] + W\frac{\partial}{\partial Z}, \quad (2.11)$$

which is now expressed in terms of a generalized vertical velocity W, defined as

$$W = \frac{S(G_1U + G_2V) + w}{G_0}, \quad (2.12)$$

where the G_i's are metric factors (Laprise 1995).

The time discretization is semi-implicit and semi-Lagrangian. The reference state is $T^* = \text{const}$ to incorporate all types of waves (gravity and elastic) in the implicit portion and to increase the numerical stability of the semi-implicit scheme (Simmons et al. 1978). Because the reference atmosphere is at rest, its pressure profile q^* is

$$\frac{dq^*}{dz} = -\frac{g}{RT^*}$$

$$q^*(z) = q_0 - \frac{gz}{RT^*}. \quad (2.13)$$

Once the perturbations (T' and q') are expanded, one can obtain the final set of governing equations for MC2:

$$\frac{DU}{Dt} + RT^*\frac{\overline{\partial q'}^t}{\partial X} = R_U, \quad (2.14)$$

$$\frac{DV}{Dt} + RT^*\frac{\overline{\partial q'}^t}{\partial Y} = R_V, \quad (2.15)$$

$$\frac{Dw}{Dt} + RT^*\frac{g_0}{G_0}\frac{\overline{\partial q'}^t}{\partial Z} - g\frac{\overline{T'}^t}{T^*} = R_w, \quad (2.16)$$

$$(1 - \alpha)\left(\frac{Dq'}{Dt} - \frac{\overline{gw}^t}{RT^*}\right) + S\left(\frac{\overline{\partial U}^t}{\partial X} + \frac{\overline{\partial V}^t}{\partial Y}\right) + \frac{g_0}{G_0}\frac{\overline{\partial G_0W}^t}{\partial Z} = R_q, \quad (2.17)$$

$$\frac{DT'}{Dt} - \alpha T^*\frac{Dq'}{Dt} + \frac{\alpha g}{R}\overline{w}^t = R_T, \quad (2.18)$$

$$\overline{w}^t - G_0\overline{W}^t = R_W, \quad (2.19)$$

$$\frac{DM}{Dt} = R_M, \quad (2.20)$$

$$\frac{DC}{Dt} = R_C. \quad (2.21)$$

The various R_i's are complex expressions holding the

explicit and nonlinear terms. In the above equations, the symbol for the total derivative has been changed to D/Dt, indicative of our use of a semi-Lagrangian scheme on three time levels,

$$\frac{D\psi}{Dt} = \frac{\psi(X, Y, Z, t + \Delta t) - \psi(X - 2\alpha, Y - 2\beta, Z - 2\gamma\mu, t - \Delta t)}{2\Delta t}, \tag{2.22}$$

where μ is a switch allowing three- or two-dimensional trajectories. In the latter case, vertical advection becomes part of the R_i's terms, expressed as a time t Eulerian operation. Interpolations required in the semi-Lagrangian scheme are made with efficient truncated bi- or tricubics whereby the higher-order terms such as $O(\Delta x^2 \Delta y^2)$ in 2D are dropped. The trajectories terminating at the central points of the MC2 molecules, the q points, are obtained from a first-order estimate of the displacement followed by two iterations of a second-order midpoint Runge–Kutta corrector. To interpolate the values of the various staggered quantities, trajectories shifted by half a grid mesh in the appropriate direction are assumed. Although we strive not to use the model at Courant numbers $\mathcal{C}$ in excess of 1.0, a small ($\varepsilon = 0.1$) off-centering of the implicit terms

$$\overline{\psi}^{t} = \frac{(1 + \varepsilon)\psi(X, Y, Z, t + \Delta t) + (1 - \varepsilon)\psi(X - 2\alpha, Y - 2\beta, Z - 2\gamma\mu, t - \Delta t)}{2} \tag{2.23}$$

is applied to reduce the problem of resonance caused by stationary forcings such as topography (Tanguay et al. 1992). Héreil and Laprise (1996) showed recently that the wrong stationary solution to the mountain wave problem due to the use of very long steps in SISL schemes, such that $\mathcal{C} > 1$, is still present in MC2; however, the scheme in MC2 is *optimal* among the currently available solutions of this resonance problem, in the sense that it distinguishes between the physical and numerical waves and keeps the best agreement for the momentum flux profile of the flow in Long's problem. It turns out that our discretization already embodies the recent Eulerian treatment of Ritchie and Tanguay (1996) for the control of orographic resonance.

The solution of the system of six equations (2.14)–(2.19) results in a three-dimensional Helmholtz wave equation for the logarithm of the pressure perturbation

$$C_1[(1 - \alpha) - (1 + \varepsilon)^2(\Delta t)^2 RT^* S\nabla^2]q' - (1 + \varepsilon)^2(\Delta t)^2 RT^* D_2[D_1(q')] = A_2, \tag{2.24}$$

involving two linear first-order differential operators:

$$D_1(q') = \frac{g_0}{G_0}\left(\frac{\partial q'}{\partial Z}\right) - \frac{\alpha g}{RT^*}q' \tag{2.25}$$

$$D_2(G_0 W) = \left(\frac{g_0}{G_0}\right)\frac{\partial G_0 W}{\partial Z} - \frac{g(1 - \alpha)}{RT^*}G_0 W. \tag{2.26}$$

The pressure equation is solved with the 3D ADI (alternating direction implicit) scheme of Peaceman and Rachford (1955) using a set of relaxation coefficients computed from the horizontal and vertical resolutions and the size of the grid, and ensuring a quasi-optimal convergence to the required machine accuracy.

The discretization of the space derivatives is by finite differences on a grid staggered in the three dimensions, which is shown in Fig. 1. This arrangement is known as an Arakawa C-grid for the horizontal and a Tokioka B-grid (Tokioka 1978) for the vertical. The center of the elementary matrix is the pressure q surrounded horizontally by U and V, and surrounded vertically by w, W, and the scalars T, M, and C. The lower boundary $\zeta = 0$ is the first w, T (thermal) level where w satisfies the adherence boundary condition $d\zeta/dt = 0$. The top boundary $\zeta = H$ is a rigid lid, $w = 0$, and a sponge layer can be applied over a certain distance below it; the last computational level is the q, U, V (momentum) half-level immediately under H.

Once the solution to the MC2 dynamics is obtained, denoted formally as ψ_{D^+}, the time-step cycle is completed by the application of the following corrections, which are computed in the manner of the fractional step method.

1) Add the nesting of the open boundaries to ψ_{D^+} to obtain ψ_{ED^+};
2) evaluate physics from ψ_{ED^+} and ψ_{D^-} and add its effects to ψ_{ED^+} to obtain ψ_{PED^+};
3) apply horizontal diffusion; and
4) apply Robert's time filter (Asselin 1972) to control

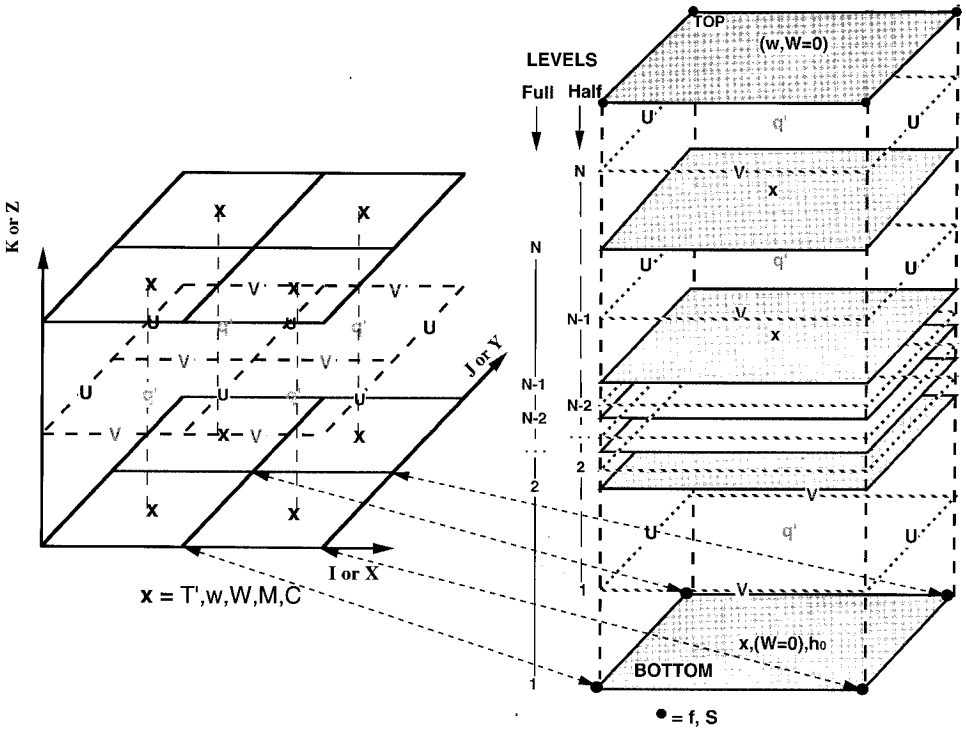

FIG. 1. The MC2 model 3D matrix of variables. Left: four neighboring cells. Right: stacking of the N basic cells over the vertical model domain, including bottom and top boundaries. Full levels holding the X points are shown with full lines while the half levels holding the Arakawa C-grid arrangement of U, V, and q' are shown with dashed lines.

time decoupling inherent to a three-time-level model. Coefficient is 0.05 usually.

Corrections 1–3 are detailed in sections 3–4.

3. Physics and interface

The MC2 model has recently been interfaced with the full unified RPN physics package. This package is shared by all operational and research models at CMC–RPN including the forthcoming GEF model. The MC2 model has also been separately interfaced with the Canadian Climate Center physics package (Caya et al. 1995) where it is now being tested in the context of regional climate studies. A warm–cold phase microphysics formulation (Zawadzki et al. 1994) has also recently been installed in MC2 and another cloudwater formulation with ice fraction has just been developed and tested in it by Tremblay et al. (1996). Another example of using the MC2 as a testbed for the development of the physics is the real-time advance testing of the combined convective–stratiform advective cloud water scheme of Sundqvist et al. (1989) during the 6-week period of the Beaufort and Arctic Storms Experiment (BASE; Benoit et al. 1995). All those physics modules will eventually reside in the same library, which should then constitute a more complete and extensive package for parameterization of a wide spectrum of physical processes.

TABLE 1. Summary of the RPN physics package.

- Planetary boundary layer based on turbulent kinetic energy
- Fully implicit vertical diffusion
- Stratified surface layer based on similarity theory
- Prediction of surface temperature over land (force–restore method)
- Diurnal cycle with solar and infrared fluxes at ground modulated by diagnostic clouds
- Solar and infrared radiation schemes fully interactive with clouds
- Shallow convection parameterization
- Kuo-type deep convection scheme
- Grid-scale condensation in supersaturated layers (with evaporation of precipitation)

a. The RPN physics package

The RPN physics package consists of a comprehensive set, with several selective options, of parameterization schemes of physical processes (Benoit et al. 1989; Mailhot et al. 1989a; Mailhot 1994). The main components of the physics package are summarized in Table 1. The package is continuously evolving and growing as new parameterization schemes are being tested and validated. The package will soon include the Canadian Land Surface Scheme (CLASS; Verseghy et al. 1993) along with more sophisticated convection schemes such as the Fritsch–Chapell (Fritsch and Chappell 1980) and the Kain–Fritsch (Kain and Fritsch 1990)

schemes. We will here briefly describe some of the physical parameterizations presently available in the current version of the package. A more comprehensive description can be found in Mailhot (1994).

Over land, the surface (skin) temperature is predicted from a heat budget using the ''force–restore'' method (Deardorff 1978; Benoit et al. 1989) combined with a stratified surface layer. Over oceans, the sea surface temperature is kept fixed during the integration. Over land, a soil moisture availability factor (percentage of field capacity) is used for calculating evaporation (Budyko bucket method or semipotential approach). This is specified from monthly climatological data.

The planetary boundary layer is based on a prognostic equation for turbulent kinetic energy (Benoit et al. 1989). A shallow convection scheme for nonprecipitating clouds is included to give a more realistic description of cloud-topped boundary layers. Shallow convection accounts for the formation of small cumuli that generally produce little precipitation but transport a large quantity of moisture vertically and play an important role in the atmospheric water cycle. Shallow convection is simulated with a method described by Mailhot (1994) and is treated as a special case of the turbulent planetary boundary layer to include the saturated case in the absence of precipitation.

Condensation processes at resolvable scales account for the formation of stratiform precipitation and, if mesh is sufficiently fine that individual convective cloud cells can be resolved, explicit convective precipitation. The explicit condensation process is simply represented by the isobaric condensation, which removes moisture when relative humidity exceeds a saturation point. The scheme includes a simplified description of microphysical processes. Advanced microphysical equations are also being incorporated in the model. No comparisons have yet been made between explicit convection and convective parameterizations included in coarser simulations.

Deep convective processes are handled with a Kuo-type convective parameterization (Kuo 1974; Mailhot et al. 1989a). A description of microphysical processes similar to that of the stratiform precipitation is also included. However, due to the complexity of evaporation from convective clouds, which strongly depends on the cloud internal dynamics (such as moist downdrafts, not included in the Kuo scheme), evaporation of convective precipitation is not considered.

The radiation subpackage contains detailed radiation schemes that are fully interactive with clouds. The infrared radiation scheme (Garand 1983; Garand and Mailhot 1990) includes the effects of water vapor, carbon dioxide, ozone, and clouds. The solar radiation scheme is essentially the one described by Fouquart and Bonnel (1980). It takes into account the effects of water vapor, carbon dioxide, ozone, clouds, Rayleigh diffusion, and multiple scattering. Cloud–radiation interactions represented in these schemes are an important effect.

Gravity wave drag parameterization is based on a simplified linear theory for vertically propagating gravity waves generated in statically stable flow over mesoscale orographic variations (McFarlane 1987). It makes use of a representation of the subgrid-scale orography (also called launching height) for exciting the gravity waves.

Vertical transfers due to turbulent air motion are parameterized in the form of vertical diffusion (Benoit et al. 1989). The effect is strongly dependent on the vertical diffusion coefficient, which is locally evaluated every time step. The vertical diffusion is especially important near the surface, but it is present over the entire atmospheric column. Delage (1988) described the difficulty of having to solve the time-dependent turbulent diffusion equation with a prognostic wind level at the surface, as done in RPN finite-element models; rather, a surface-layer diagnostic (SLD) routine is made part of the physics package. The SLD gives a diagnostic (i.e., not derived from a time-dependent differential equation) value of the state of the surface-layer variables (only u, v, T, and humidity) at any reasonable height, based on the current surface stress and turbulent fluxes determined from the rest of the boundary layer scheme, and on some simple assumption on the low-level profiles. Also, vertical diffusion is modified in many RPN models (including MC2) to control excessive divergence near the top of the models. The actual artifice used is simply to increase the momentum vertical diffusion coefficients on the four highest computational levels.

b. Initial and boundary conditions

A number of fields and parameters are needed to specify the surface characteristics and are obtained from analyses and climatological and geophysical datasets. These include surface roughness, land–sea mask, albedo, deep soil temperature, ice cover, and orography. The surface roughness length is influenced by orography and vegetation. The snow cover is incorporated only into the albedo field. Other surface parameters are tabulated as functions of a soil or surface type index. For the moment, this index is the same for all land points. The soil parameters are representative of a clay soil, which is considered to be reasonably applicable over North America. Our group has recently acquired a forest map/land cover database at 1 km, truly seamless and complete for all of the Canadian landscape (Palko et al. 1996). This is based on Advanced Very High Resolution Radiometer (AVHRR) imagery from National Oceanic and Atmospheric Administration (NOAA) polar orbiters and was assembled as part of the National Atlas Information Service of Canada.

A set of mutually consistent ''geophysical'' parameters is required to initialize the RPN physics package. This set currently includes the following.

1) Time-invariant quantities
   - mean terrain height;
   - launching height;
   - land–sea mask; and
   - roughness length for the turbulent surface fluxes.
2) Time-dependent quantities, either from monthly climatology or gridded from the observations valid at initial time
   - surface temperature (land or sea surface);
   - deep soil temperature;
   - soil wetness;
   - snow fraction on ground (for albedo modification only);
   - sea ice; and
   - surface albedo.

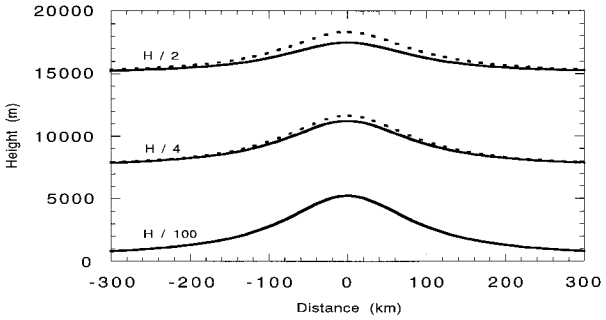

FIG. 2. Three Gal-Chen surfaces (solid) and the corresponding σ surfaces (dashed) over a 5000-m idealized mountain shape. Here H is the model lid (32 000 m). Curve labels are the value of the Gal-Chen coordinate.

c. Connecting with the dynamics—Physics interface

The main purpose of the current MC2 interface with physics is to run the RPN physics package in order to obtain parameterized tendencies for the two horizontal components of the wind, the temperature, the humidity, and the cloud water content; these are the F_i terms of Eqs. (2.1)–(2.7). To achieve that goal, the interface imbedded in the MC2 time loop must carefully prepare the input data fields from the dynamics, run the physics, and consistently postprocess the different tendencies before adding them to the respective dynamic fields. The physics package is designed to operate on a set of completely independent atmospheric columns. This simple but crucial assumption allows for the possibility of parallel computing and must therefore carefully be taken into account in the design of the physics interface. The physics configuration (selective options) and the geophysical fields needed for a particular configuration are acquired once at the first time step.

1) PREPROCESSING THE DYNAMICS FIELDS

The basic requirements of the RPN physics package in terms of input data from the dynamics are the three components of the wind, the temperature, the humidity, and the cloud water content, all collocated on a single set of vertical levels with one level at the surface. Each of these fields must be provided for two time levels corresponding to the state of the variables at $t - \Delta t$ and the state after they have been updated by the dynamics time step, respectively. Since the dynamics is on an Arakawa C-type staggered grid (Fig. 1), we have opted to run the physics on the temperature points and consequently to interpolate in three dimensions the horizontal components of the wind onto the temperature points. This choice was mainly motivated by coding simplicity rather than actual physics considerations, and other avenues are being investigated. Each 3D matrix of the dynamics is transposed vertically because the computational levels within the physics package are ordered from top down (pressurewise indexing), the opposite of the MC2 dynamics (heightwise indexing).

The last step that needs to be completed before running the physics is to compute and provide the physics with the local σ value of every point of the MC2 3D temperature mesh. This step is required because the RPN physics package was developed for models using a σ vertical coordinate and is still operating on that vertical coordinate in the current version. For the moment, σ values are computed by vertically integrating the hydrostatic equation from the surface up to each of the computational levels using a simple trapezoidal rule. The difference between Gal-Chen and σ terrain-following surfaces is depicted in Fig. 2 where the height of the three surfaces are compared. It can be seen that Gal-Chen surfaces are very parallel to sigma surfaces in the low levels of the atmosphere. Aloft, they behave like the hybrid σ–p coordinate [such as in the European Centre for Medium-Range Weather Forecasts (ECMWF) model] since they flatten out and eventually become horizontal at the model top H, contrary to the sigma surfaces that retain their curvature at all levels.

At this stage, the physics package is ready to be run. This computational task can be concurrently dispatched to several processors (when the model is executed on a multi-CPU, $O(10)$, shared-memory computer) because of the previously mentioned column-independent structure of the physics package. At the very end, when the physical parameterizations have been computed for all columns, the physics package will return to the interface a whole series of separate tendencies for all the different physical processes of the current configuration. Those tendencies need then to be combined appropriately in order to obtain global physics tendencies for the two horizontal components of the wind, the temperature, the humidity, and the cloud water content.

2) HANDLING THE TENDENCIES DUE TO PHYSICS

The global 3D physics tendency matrices need now to be vertically transposed again to obtain values on computational levels ordered from the bottom up. Fur-

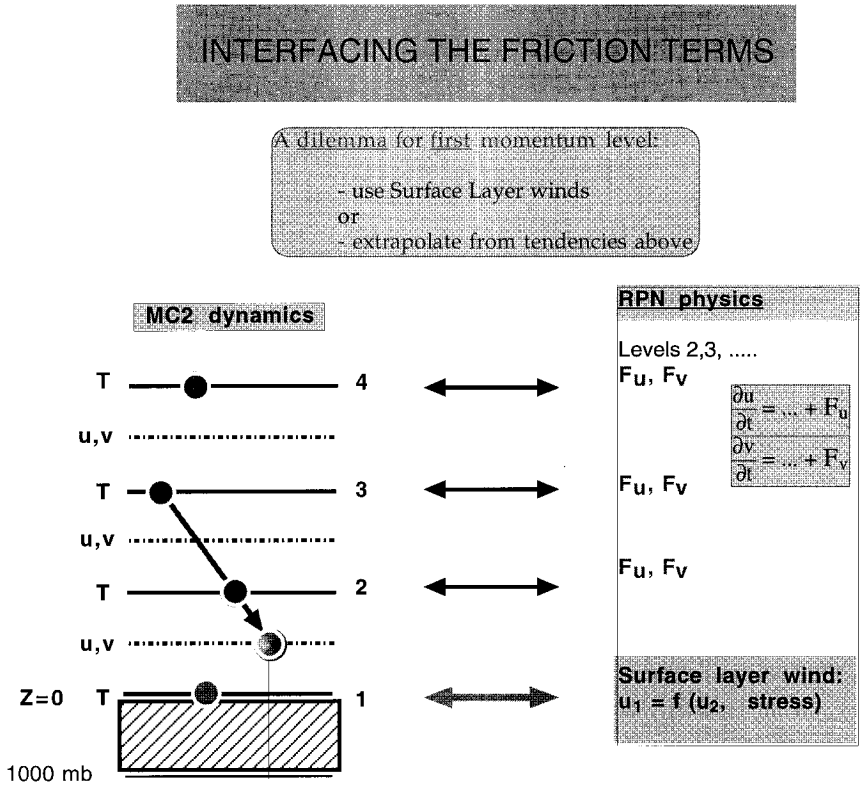

FIG. 3. Schematic illustrating the dilemma to be resolved for the calculation of the tendency values due to the RPN physics for u and v on the first momentum level. This physics package requires a data level at the surface $\sigma = 1$. The dots indicate raw tendencies returned by the physics on the thermodynamic levels T.

ther, the two tendencies for the horizontal components of the wind, F_u and F_v, have to be horizontally and vertically staggered back to the u and v grids, respectively. Vertical staggering from thermodynamic to momentum levels will leave the top momentum level undefined and we chose to impose F_u and F_v on that level to equal the tendencies directly received from the physics on the top thermodynamic level. On the lowest thermodynamic level, the surface layer, the physics tendencies are computed differently, by calling the SLD routine to directly compute wind, temperature, and humidity at time $t + \Delta t$. Since the first MC2 prognostic wind level is not at the surface but half a layer up, there is no real justification here for the SLD approach and a kind of dilemma arises, as depicted in Fig. 3. To obtain tendency values for u and v on the first momentum level, we have the choice of either linearly weighting the tendencies between the first two thermodynamic levels (thus using SLD) or extrapolating from tendencies on thermodynamic levels 2 and 3 (thereby ignoring SLD). The latter option was chosen because of a problem that was diagnosed for at least one case and that will be briefly discussed in section 5a. Note that this difficulty does not arise for the temperature and humidity also computed by the SLD scheme, since no vertical displacement of the results is required for those two quantities. Furthermore, the full impact of the surface stress and its variation with inhomogeneous roughness are felt by the MC2 via the vertical diffusional tendencies received on thermodynamic levels 2 and upward because the surface stress is the flux (Neumann) lower boundary condition to the diffusion differential equation.

Finally, the global physics tendencies are horizontally nested to zero within the horizontal sponge zone (see section 4) before being added to the respective 3D dynamic matrices. This nesting will damp, in a consistent manner, the effect of the physics parameterization in the horizontal sponge zone of the domain, therefore preventing strong physics tendencies to be applied in that particular part of the domain. This corresponds to assuming that the external fields used as lateral boundary conditions are already properly balanced in terms of physics. This completes step 2 of the fractional step method.

3) HORIZONTAL DIFFUSION

The last step (step 3 of the fractional step method) in the physics interface is the horizontal diffusion that is actually performed on the eight dynamic prognostic variables. In order to have a horizontal diffusion coefficient that is automatically adjusted to the grid res-

TABLE 2. Values of horizontal diffusion factor N for dynamics variable F; each of the eight F symbols corresponds to the main variable in Eqs. (2.1)–(2.7) and (2.12), respectively.

F	N
U	1
V	1
w	5
q	1
T	1
M	1
C	1
W	5

olution, we define a *dimensionless viscosity*, η, related to the effective horizontal diffusion coefficient K_h by the relation $K_h = (\eta \Delta x^2)/\Delta t$, where Δx is the size of the grid mesh and Δt the time step; η is usually taken as 1.44×10^{-2}, which gives a diffusion coefficient similar to the one used by the 50-km RFE model of CMC. The horizontal diffusion operator is applied to a generic field, F, according to the relation $\partial F/\partial t = NK_h\nabla^2 F$ where the horizontal diffusion factor N is given in Table 2, depending on which field is being diffused. The diffusion equation is solved with a fully implicit time scheme (Jakimow et al. 1992). More rigorous studies on atmospheric viscosity suggest that K_h should be independant of time step (e.g., Bartello et al. 1996)

4. Nesting and initialization aspects

a. The current one-way nesting

MC2 being a limited-area model, it is necessary to specify the lateral and upper boundary conditions at every time step. Inspired by Davies (1976), the nesting method used in MC2 was actually developed by Robert and Yakimiw (1986) and Yakimiw and Robert (1990). Horizontal and vertical nesting is performed on all the predictive variables except the cloud water content (this exception must be overcome in self-nested applications that include the cloudwater). It is carried out over a user-defined sponge zone once the variables have been updated by the dynamics time step. In the horizontal, the sponge zone consists of a number of grid points ($L_x + 1$, $L_y + 1$) from the lateral boundary. The nesting values Ψ_n are gently and gradually blended with the values Ψ_d obtained from the dynamics time step according to the equation

$$\Psi_R(i, j, k) = P(i, j)\Psi_n(i, j, k) + [1 - P(i, j)]\Psi_d(i, j, k). \tag{4.1}$$

Here Ψ_R is the resulting nested field and P is the attenuation function, which is defined as follows along the x axis (j = const):

$$P(i,j) = \begin{cases} \cos^2\left(\dfrac{\pi}{2}\dfrac{i-1}{L_x+1/2}\right), & 1 \le i \le L_x + 3/2 \\ \cos^2\left(\dfrac{\pi}{2}\dfrac{ni-i}{L_x+1/2}\right), & ni - L_x - 1/2 \le i \le ni \\ 0, & \text{elsewhere.} \end{cases} \tag{4.2}$$

A similar expression for P is used along the y axis and a value combined from both expressions is applied in the corners of the grid. Figure 4 shows the attenuation function P on a 51×51 grid with $L_x = 7$ and $L_y = 12$. Different L_x and L_y have to be allowed in a general modeling system for the case of ''small'' rectangular grids where ni and nj are sometimes very different and one of them is $O(10)$, such as for approximating a plane-parallel (x, z) problem. It can be noted that ∇P is null at the interface between the horizontal sponge zone and the free internal domain. Transition between nested and nonnested values will therefore be smooth, providing that enough grid points are used in the sponge zone to resolve the attenuation function P properly. Since eight grid points are usually considered to be enough to resolve one full wavelength numerically, it is suggested that ten grid points are enough to blend smoothly the external values with the ones from the dynamics time step using the attenuation function defined in (4.2). Thus, the general practice with MC2 on ''large'' grids is to take $L_x = L_y \sim 10$, whereby the attenuation function is well sampled.

In the vertical, the sponge zone is a layer of depth L_z under the model lid. Vertical nesting is performed in the same manner as horizontal nesting [Eq. (4.1)] but with an attenuation function P_z defined as

$$P_z(k) = \begin{cases} a\left\{1 - \min\left[1.0, \dfrac{Z_{\text{top}} - Z(k)}{Z_{\text{top}} - H + L_z}\right]\right\}^2, \\ \qquad Z(k) > H - L_z \\ 0, \qquad Z(k) \le H - L_z, \end{cases} \tag{4.3}$$

where $Z(k)$ is the height of the kth computational level, Z_{top} is the height of the highest computational level, H is the model lid ($>Z_{\text{top}}$), and a is a constant taking value between 0 and 1 ($a = 0.2$ in the current version).

Vertical nesting used here is quite different from the method described by Burk (1989) for the limited area Navy Operational Regional Atmospheric Prediction System (NORAPS). In that model, the dynamics time step is performed on a coarse vertical grid and the physics on a finer vertical grid with the same vertical extent. A double vertical interpolation is performed at every time step to run the physics on the fine grid and to return the tendencies on the dynamics coarse grid. As usual, the model lid must be set high enough to satisfy the constraint of zero vertical motion at the top of the model. In the MC2 model, the dynamics and the physics operate on the same computational levels. The vertical nesting

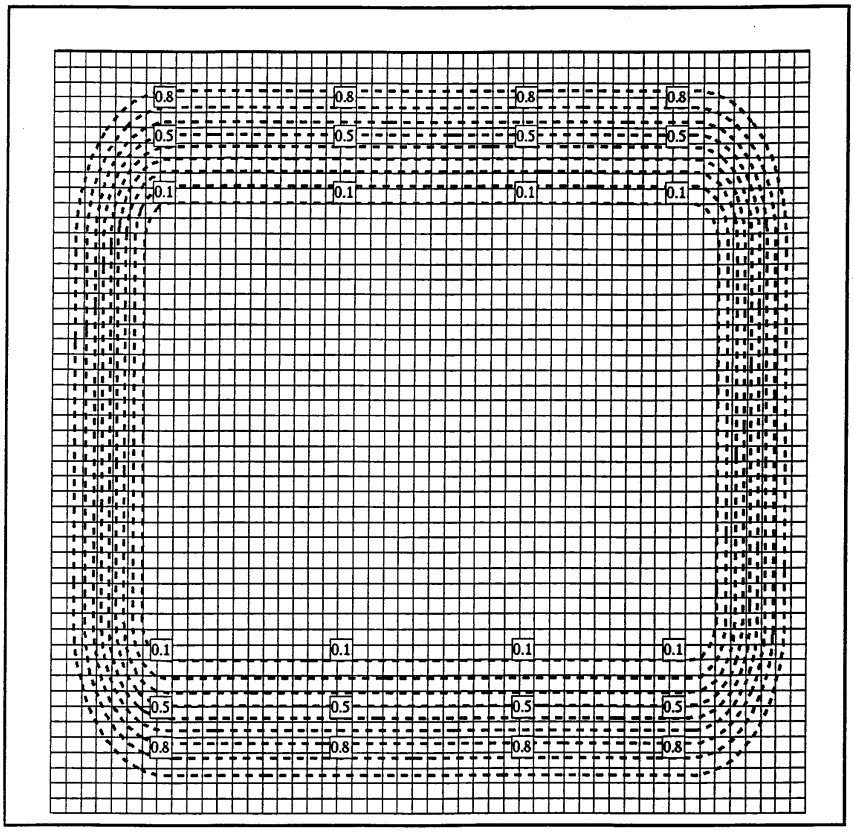

FIG. 4. The attenuation function P for the lateral nesting. The sample grid is 51×51 and $L_x = 7$, $L_y = 12$.

allows one to set the model top lower in the troposphere, thereby concentrating the whole computational effort on a smaller vertical domain. On the other hand, vertical nesting can be used to control gravity wave reflections at the model top by simulating an absorption layer in which upward propagating wave energy will be dissipated.

As can be seen from Eqs. (4.2) and (4.3), vertical nesting will not be performed at all when $L_z \leq (H - Z_{\text{top}})$, that is, when the nesting layer does not reach the topmost momentum level, contrary to the horizontal nesting, which is always performed at least on the horizontal boundary even if $L_x = L_y = 0$.

It is therefore necessary to provide the model with sets of nesting values for all the dynamics variables, valid at regular time intervals, to cover the whole integration period. Linear interpolation in time between two consecutive sets of nesting data will be performed by the model to obtain the required nesting values for a particular timestep. Nesting values often consist of output data obtained from another larger-scale model such as the Canadian RFE or the Canadian Spectral Finite Element (SFE) model, but they may also consist of a set of objective analyses covering the integration period. Finally, output data from a previous run of the MC2 model itself may be used as nesting values for a subsequent run, possibly at higher resolution. This self-nesting (or cascade) capability of the MC2 model is a very useful feature when trying to run the model at very high resolution starting with initial analysis available only at much coarser resolution. It has the advantage of optimizing the dynamical consistency between the coupled models. This is demonstrated further in section 5.

b. Initialization

The MC2 model uses a type of dynamic initialization. This simple scheme is performed by first integrating the model forward in time for a small, $O(10)$, number of timesteps (without physics) and then backward to the starting time to begin the forecast itself. As in other models, the initialization timestep is usually smaller than the one used for the regular integration; for example, Temperton and Roch (1991) take an initialization timestep of 120 s in the application of a nonlinear normal mode initialization (NLNMI) to a baroclinic semi-implicit 3D model whose main time step is 1200 s. In the NLNMI, the small time step is theoretically required to eliminate the false response of the semi-implicit scheme for the gravity waves that are being initialized, and in practice it improves the convergence of the meth-

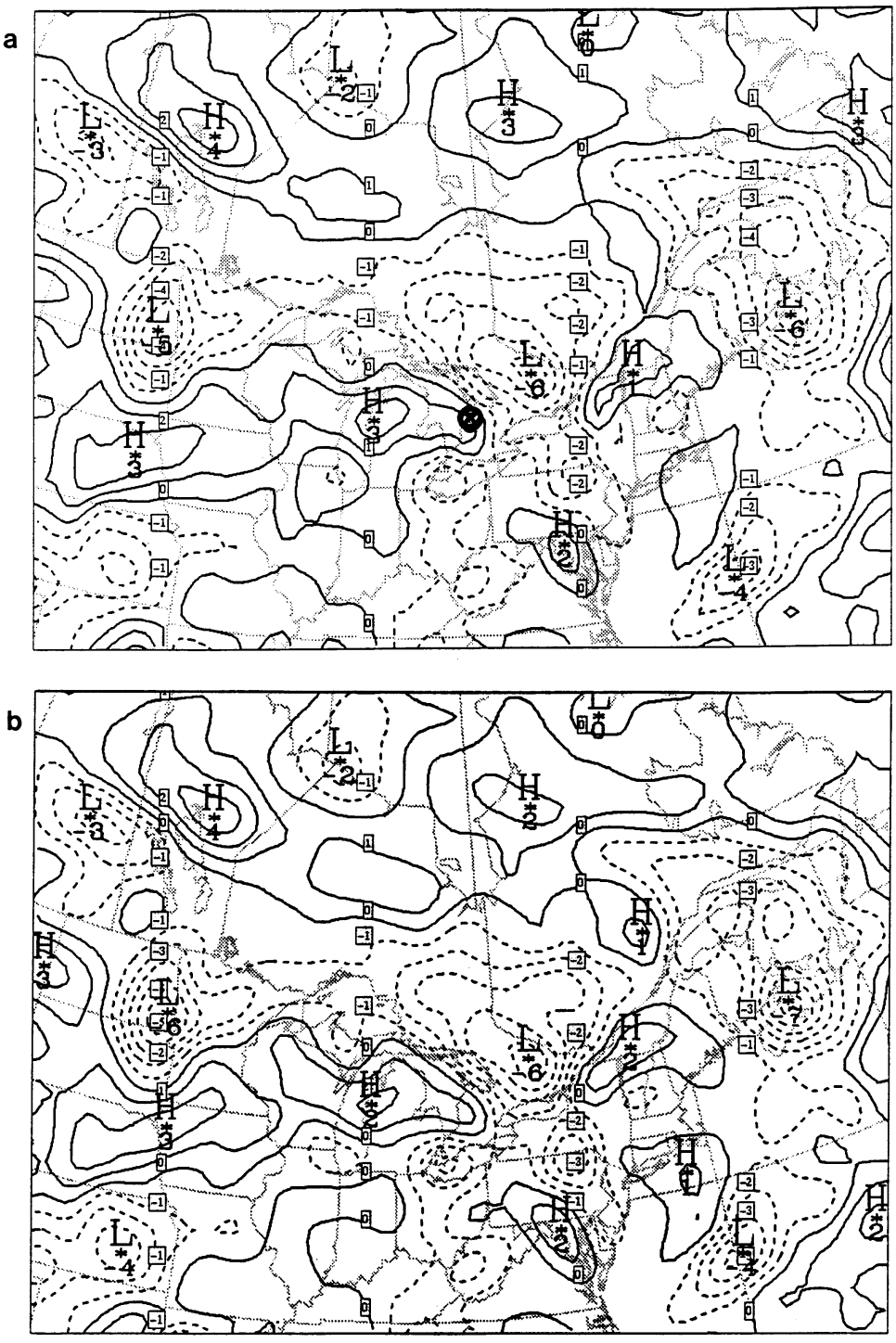

FIG. 5. The 500-hPa vertical motion, contoured every 1×10^{-1} Pa s^{-1}, after initialization of the (a) MC2 and the (b) RFE models. Dashed lines indicate negative values.

od. MC2 is also semi-implicit, but the justification of the small step has not been examined yet.

Initialization is used whenever there is doubt about the balance state of the initial conditions or when a field such as vertical motion is not provided in the initial analysis, as is often the case with most current data assimilation systems. It is in fact very often difficult to start an integration with an initial vertical motion that is perfectly balanced with the other dynamical fields even if the initial conditions come from a previous run

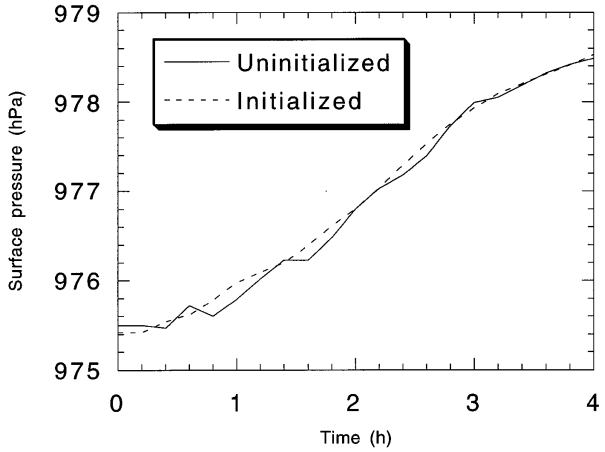

FIG. 6. Effect of initialization on time traces of surface pressure at grid point denoted by a heavy dot on Fig. 5a.

by another model. This is partly due to the fact that vertical interpolation of input data to the MC2 computational levels tends to disrupt the balance of the input dataset. Moreover, it would be incorrect to assume that the balance state of any set of input data, be it an objective analysis or model output, is compatible with the precise numerical balance of the model to be initialized with such data. For that reason, we tend to omit the initialization on the finer meshes when these are driven by a coarser MC2 run.

A sample of the effect of this simple dynamic initialization scheme is depicted in Fig. 5, which shows the vertical motion after initialization of both the MC2 and the RFE models. The two models were run at 50-km horizontal resolution and on 25 vertical levels, with a 720-s time step. The CMC objective analysis of 0000 UTC 13 January 1995 (no vertical motion in the analysis) was used as an initial condition for both models, and each employed its own initialization scheme. The RFE model uses a normal mode initialization, while, for this particular case, the MC2 model performed a four-time-step dynamical initialization with a 360-s time step. The remarkable similarity between the vertical motions developed by the two initialization schemes is a clear indication of the validity and utility of a very simple dynamic initialization scheme. In a more classic manner, the effect of initialization can also be seen in time series of surface pressure at selected points of the domain (Fig. 6). In general, initialization is very helpful in reducing the spurious pressure oscillations that usually occur during the beginning of an integration (first 3 h in this case) and can reduce the so-called (condensation) spinup problem. Note that the effect shown here is mostly related to the external gravity mode, easiest to control; we make no claim that our simple scheme has a significant effect for the internal modes.

Vertical interpolation for the initial and lateral boundary conditions is cubic from z (height above sea level) to ζ. Input can be in pressure, sigma, Gal-Chen, and

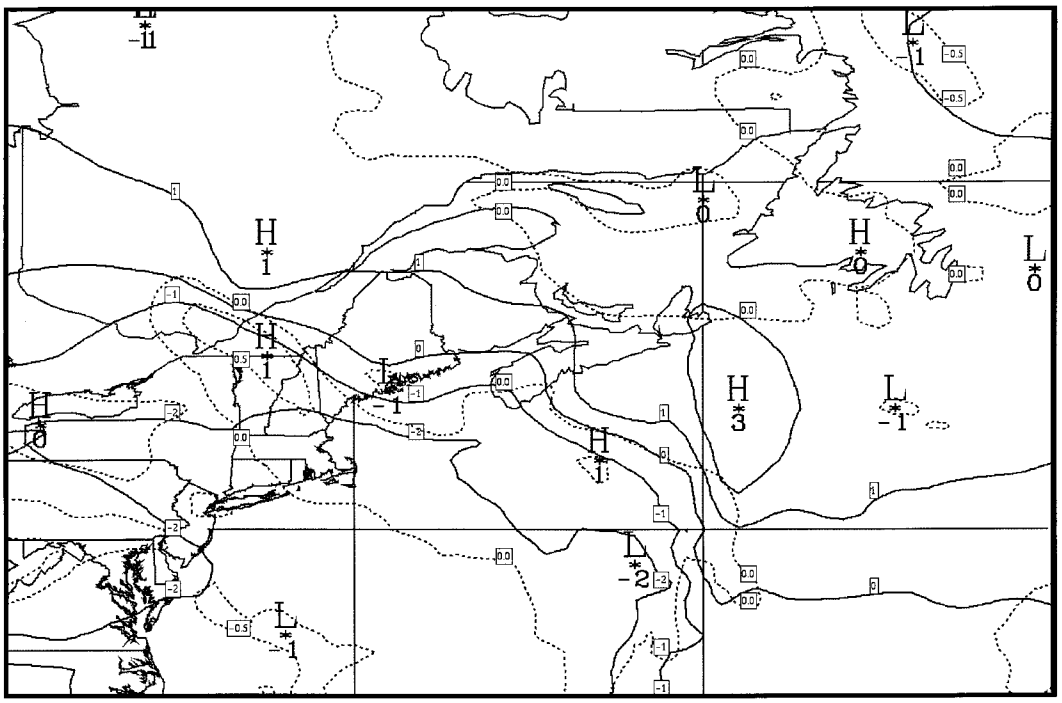

FIG. 7. The difference (simulation mode minus forecast mode) between the two 24-h solutions for mean sea level pressure (solid lines), contoured every 1 hPa, and the 10-m temperature (dashed lines), contoured every 1°C, for the two runs over a verification domain (domain C of Fig. 9).

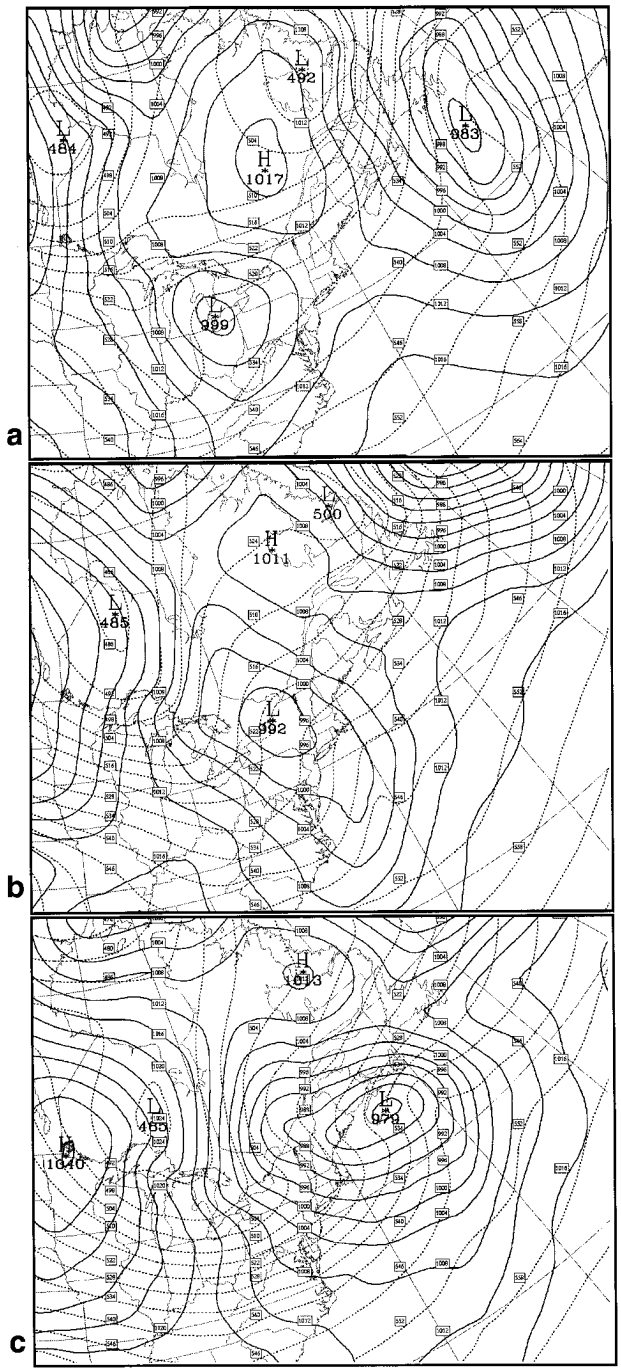

FIG. 8. CASP 1 IOP 14 analysis for COMPARE 1 valid at (a) 1200 UTC 6 March, (b) 0000 UTC 7 March, and (c) 1200 UTC 7 March 1986. Mean sea level pressure (solid) contoured every 4 hPa and 1000–500-hPa thickness (dashed) contoured every 6 dam.

hybrid (eta) coordinate. Output is cubically interpolated to pressure levels, or the raw Gal-Chen levels can be output for cascade purposes.

To complete this subsection, let us summarize our nesting philosophy for cascade runs. First, the characteristics of the finest integration are chosen (domain size, mesh, duration) according to the phenomenon being examined and available data/resources. Then we design the sequence of coarser runs that will enable the zoom to this finest run. The ratio of nested grid meshes is taken between about 2 and 5; MC2 users have not found sensitivity to this factor and the results shown below are with values of 3 and 5. The coarsest grid is usually chosen to have a mesh corresponding with the resolution of the coarsest source of gridded atmospheric analysis available for the given problem. The vertical interpolation to pass from one grid to the next finer one is done directly in a Gal-Chen coordinate, with proper accounting for the displacement of the terrain elevation on the target grid caused by the injection of finer-scale physiographic/topographic fields. The different grids are run sequentially and not in parallel to give further possibility of adjusting slightly the features of the remaining grids based on the obtained simulation. A time shift of the starting time is introduced between consecutive grids to cover the spinup time of adjustment of the fields to the changed terrain.

c. Simulation and forecast modes

The ideas of this section are presented in the context of atmospheric modeling over a quasi-hemispheric domain, to account for the present MC2 limitation to conformal mapping coordinates: at this stage, latitude and longitude coordinates are not implemented and this prevents us from using the full global domain. With the corresponding application of lateral boundary conditions near the equator, it is clear that the strategy explained here cannot avoid increased error level in the lower Tropics.

The MC2 model can be run in two basic modes, depending on the origin of the lateral and upper boundary values used for nesting. These are the *simulation* mode and the *forecast* mode. In the simulation mode, a series of gridded analyses or output fields from a previous run by another model will be used as nesting values. One can then argue that, in this mode, the model is somewhat forced toward a particular solution because we impose on it a known or previously forecast solution via the nesting sponge zone. In the true forecast mode, the model starts with only gridded analysis valid at initial time and produces a forecast without ever using data from the (still) future state of the atmosphere on the lateral and upper boundary; in this mode, the model is self-sufficient and does not rely on any other forecast model. If the forecast is made with a nest of several meshes, then it is preferable to start each nested grid from a distinct analysis gridded on the corresponding resolution, as in the example below; this is important to represent the smaller-scale transient/nonforced features in the initial conditions of the model. It is claimed here that MC2 can currently operate in the true forecast mode for time periods relevant for regional models, that is, about 2 days, as long as the region of interest is away

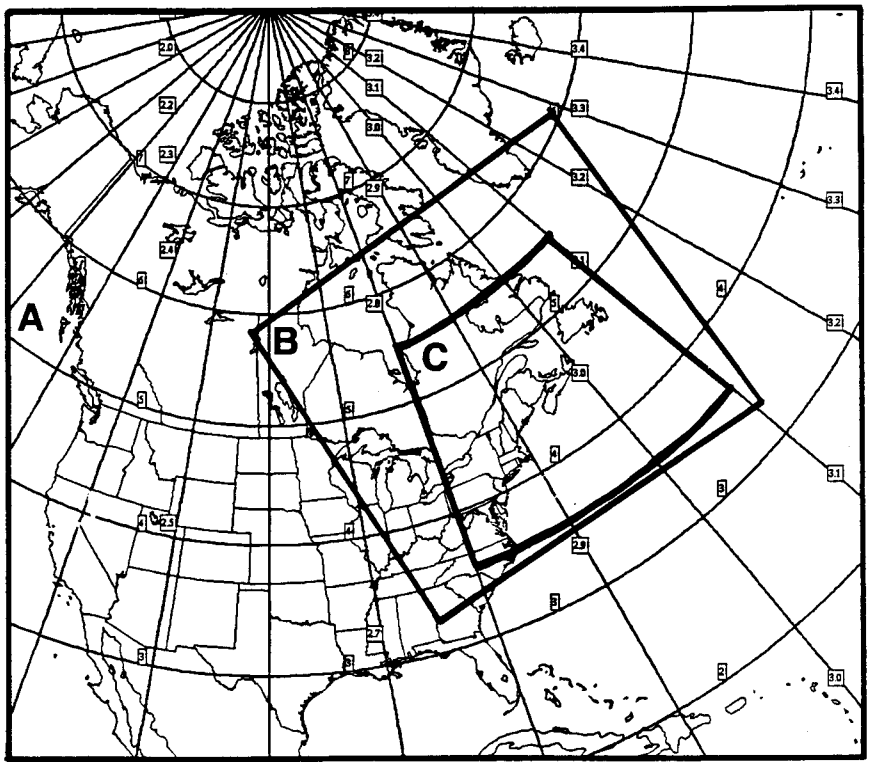

FIG. 9. Domains for COMPARE 1 protocol. Domains A and B are (MC2) integration domains, while domain C is the verification domain.

from the equator. To go beyond that range or to relax the geographical constraint would at least require having spherical coordinates in MC2 to allow full global interaction and/or pole translation. The basic idea is first to perform a coarse-resolution hemispheric run for which the (equatorial) lateral conditions are kept constant at their initial value throughout the whole integration period. This constraint is not really of big concern because the objective is to cascade the model at higher resolution over a subdomain that will most of the time be far away from the equator. Moreover, synoptic conditions at the equator do not change all that much over a 24–48-h period, which suggests that a constant state of the atmosphere might by itself be an acceptable solution over such a period of time. This strategy is also not very different from the one used by other hemispheric models such as the RFE, which imposes solid wall conditions on the periphery of its domain; this wall boundary condition is also maintained without reported difficulties in the regional data assimilation spinup cycles initiated from a global assimilation cycle for the RFE (Mailhot et al. 1995a). Allowing time-independent inflow/outflow boundaries near the equator poses no difficulty with MC2 and should be somewhat more realistic than a solid wall.

To demonstrate this point, the MC2 is applied on one of the two cases that are used extensively in section 5 below on applications of the model. The simulation and forecast modes have been tested using the Canadian Atlantic Storm Project 1 (CASP 1) IOP 14 case of 6 March 1986 for which a global analysis at 1° resolution and a regional analysis at 50-km resolution were available every 6 h. The synoptics and meteorology of this case are briefly discussed in section 5a of this paper. The MC2 was run in both modes for a 36-h forecast at a horizontal resolution of 50 km over domain A of Fig. 9. In both integrations, the number and placement of the computational levels, along with the dynamics and physics configuration, were identical. In the forecast mode, the hemispheric run, at a resolution of 150 km, was initialized with the *global* analysis of 1200 UTC 6 March, while the *regional* analysis valid at the same time was used as initial conditions for *both* 50-km runs. In simulation mode, the nesting conditions were provided by the subsequent regional analysis at every 6 h. In forecast mode, the nesting values consisted of output data every 6 h of the previous hemispheric MC2 run. Figure 7 shows the difference (simulation minus forecast) between the 24-h forecasts of mean sea level pressure and 10-m temperature for the two runs over a verification subdomain (domain C of Fig. 9). One can see that the two solutions are in general very similar, which seems to indicate that the model can be run in any of the two modes with the same degree of confidence. In this particular case study, however, it seems that the forecast mode better predicted the position of the sec-

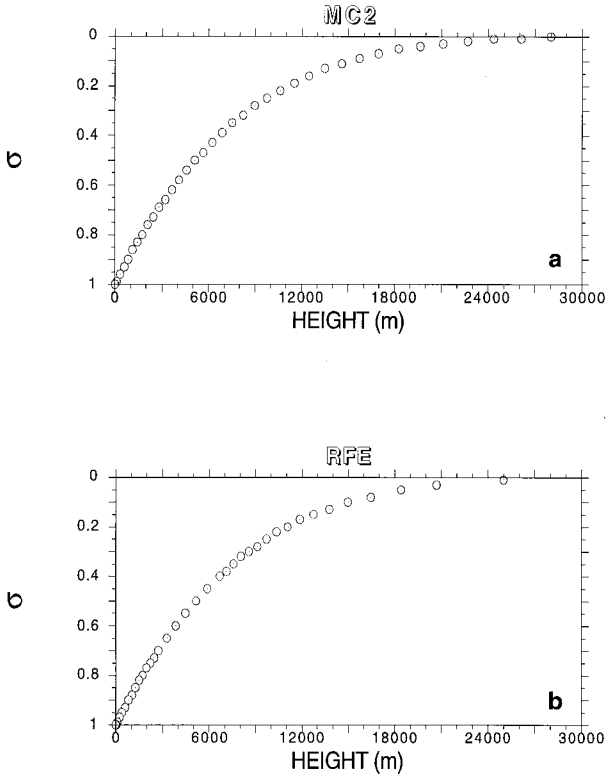

FIG. 10. The distribution of vertical levels for the COMPARE 1 experiment 2 as (b) originally proposed and as (a) actually used by MC2. Height above sea level computed for a constant lapse rate atmosphere for levels over sea.

ondary cyclone southeast of Nova Scotia by moving it a little farther to the northeast than the simulation mode (see analyses in Fig. 8 and simulation run in Fig. 10).

Table 3 provides detailed comparative cost figures for the case under consideration here, that is, the 50-km forecast for the CASP 1 IOP 14; both models are assumed to have similar computational efficiency. In forecast mode, the computational overhead of having an additional hemispheric 150-km run to perform in order to produce a 36-h forecast at 50 km is minimal at 0.29 units (one unit is the cost of the main calculation at 50 km), because of the longer time step, 1800 s. The cost with the variable resolution strategy of the RFE model with a central domain [domain A of COMPARE (Comparison of Mesoscale Prediction and Research Experiment)] corresponding to the whole MC2 computational grid, at the same horizontal and vertical resolution and with the same timestep, is 1.89 units. The overall computational cost of the two MC2 runs is 1.29 units, roughly 32% less than 1.89, the computational cost of the single RFE model run. This is mainly due to the fact that the variable resolution grid forces the RFE to process about 89% more grid points than the MC2 ($=M^2$). These points must be computed with the 50-km time step (600 s) even though the RFE resolution reaches approximately 1000 km near the equator in this configuration. The average resolution within the variable portion is about 250 km, computed as (23 000 − 8000)/60, which is less than in the MC2 hemispheric run, 150 km.

5. A few applications

Since its delivery to the scientific modeling community in February 1994, the MC2 model has been used to simulate a wide variety of meteorological features ranging from large-scale extratropical storms (50–100-km mesh) to smaller mesoscale events (2-km mesh and less). The MC2 model has also been used as a real-time high-resolution forecast model in support of the field phase of BASE, which took place from 1 September 1994 to 31 October 1994 (Benoit et al. 1995). Other studies such as high-resolution distribution of precipitation over the Columbia River basin in southern British Columbia (Mailhot et al. 1995b), lake-driven circulation, mesoscale precipitation bands, surface wind storms, and others are currently being completed. We will discuss here only two applications of the MC2 model involving simulations of a large-scale coastal development and of a mesoscale nonhydrostatic downwind storm.

TABLE 3. Cost comparison of MC2 and RFE on COMPARE case forecast at 50 km; domains defined on the polar stereographic plane true at 60°N. Location of "A" is given in Fig. 9.

Model	Mesh length (km)	Time step (s)	Grid size	Domain	Cost (relative)	Remarks
MC2	150	1800	$150 \times 150 = 0.88M^2$	Hemisphere = (23 000 km)^2	0.29	$= (150/160)^2 \times (600/1800)$
MC2	50	600	$160 \times 160 = M^2$	A = (8000 km)^2	1 unit	= Unit of cost M^2 = unit of grid size
Total MC2					1.29	sum of two grids
RFE =			220×220	Hemisphere	1.89	size of full grid
Central	50	600	$160 \times 160 = M^2$	A		same region as for MC2
+						
Exterior	50–1000	600	$4(30 \times 160 + 30 \times 30) = 0.89M^2$	Hemisphere minus A		• stretched portion: stretch ratio = 1.1 • 4 (side + corner)
Total RFE					1.89	$= (220/160)^2$ single grid

TABLE 4. COMPARE 1 participants.

Country	Model	Type	Projection	Vertical coordinate
Canada	MC2	Nonhydrostatic	PS	Gal-Chen
Canada	RFE	Hydrostatic	PS	σ
United States	ETA	Hydrostatic	L	Step-mountain (eta)
United States	FSU (global)	Hydrostatic	L	σ
United States	MM4	Hydrostatic	PS	σ
United States	PSU/NCAR	Hydrostatic	PS	σ
United States	UW/NMS	Nonhydrostatic	L	z
France	PÉRIDOT	Hydrostatic	PS	σ
Italy	BOLAM	Hydrostatic	L	σ
Australia	CSIRO	Hydrostatic	PS	σ
Japan	JMA	Hydrostatic	PS	σ
United Kingdom	UNIFIED	Hydrostatic	L	Hybrid

a. The first COMPARE case: CASP IOP 14

The COMPARE project is an international community effort in mesoscale modeling whose goals are to understand further mesoscale predictive capability, identify important issues of mesoscale research, and establish over the years a testbed of a broad range of mesoscale cases using high-quality raw datasets, assimilation systems, and analyses (Gyakum et al. 1995; Gyakum et al. 1996). The first case selected for the COMPARE project is an explosive marine cyclogenesis case that occurred 6–8 March 1986 over the North American east coast. A very good database is available for that case because the storm was covered by an intensive observation period of the Canadian Atlantic Storms Program (CASP; Stewart et al. 1987) and the Genesis of Atlantic Lows Experiment (GALE; Dirks et al. 1988). Chouinard et al. (1994) reviewed the existing literature. Some 12 models belonging to seven countries of the international modeling community participated in this first COMPARE experiment (see Table 4). Among all participants, the MC2 (using a Gal-Chen vertical coordinate) and the University of Wisconsin NMS (using a height vertical coordinate similar to eta) models were the only nonhydrostatic models.

The first COMPARE case study (CASP 1 IOP14 case of March 1986) is a spectacular example of wintertime oceanic explosive cyclogenesis with a maximum deepening rate of 18 hPa $(12\ \text{h})^{-1}$ occurring between 0600 and 1200 UTC 7 March. By 0000 UTC 7 March, a cyclone, having formed two days earlier in the lee of the Canadian Rockies, had traveled eastward to the Lake Erie area (Fig. 8). At this time, a secondary low pressure center was developing off the coast just south of Long Island in the trough extending from the parent low. During the next 12 h this coastal cyclone intensified rapidly as it moved northeastward across the strong sea surface temperature (SST) gradient of the Gulf Stream. By 1200 UTC 7 March the central pressure had deepened to 979 hPa as the storm was approaching southeastern Nova Scotia. The storm then traveled across the Gulf of St. Lawrence and gradually occluded. As discussed by Mailhot and Chouinard (1989), the surface cyclone intensified downstream of a mobile upper-level trough and below the entrance region of the jet. A low-level jet (LLJ) with high moisture content was also present in the warm sector just ahead of the cold front (Chouinard et al. 1994).

1) METHODOLOGY

Included in the COMPARE 1 distribution package was a set of analyses at 6-h intervals covering the period from 1200 UTC 5 March to 0000 UTC 8 March 1986, on a 50-km resolution polar-stereographic domain covering most of North America (domain A of Fig. 9). Data was provided on 44 equally spaced vertical isobaric levels.

The MC2 group performed the first five out of seven proposed experiments aimed at studying the issues of horizontal and vertical resolution. The focus for all experiments was a 36-h forecast commencing at 1200 UTC 6 March 1986. The proposed experiment 1 is at a horizontal resolution of 100 km over domain A of Fig. 9 and with the following positions for 18 computational levels in σ: 0.01, 0.05, 0.1, 0.15, 0.20, 0.25, 0.30, 0.35, 0.40, 0.50, 0.60, 0.70, 0.75, 0.80, 0.85, 0.90, 0.95, and 1.0. Experiments 2, 3, and 4 would be run on the same horizontal domain and would respectively double vertical resolution (100 km, 35 levels), double horizontal resolution (50 km, 18 levels), and double both horizontal and vertical resolutions (50 km, 35 levels). The suggestion for the placement of levels was to insert one additional level in each of the layers used in experiment 1. Experiment 5 aimed at *quadrupling* the horizontal resolution and *tripling* the vertical resolution (25 km, 52 levels), and it was suggested that two additional levels be inserted in each layer used in experiment 1. Because experiment 5 is an expensive high-resolution computation, it was necessary to run it on a reduced-size domain (corresponding approximately to domain B of Fig. 9) and for a shorter time period. Results were to be returned at 6-h intervals on a lat–long verification domain (grid C of Fig. 9) at 0.5° resolution and on 20 equidistant isobaric levels. The time steps used for the various experiments are, respectively, 1200, 600, and 300 s for horizontal resolutions of 100, 50, and 25 km.

TABLE 5. Physics configuration. [Full RPN/CMC physics package (version 3.0).]

Surface physics (land: force–restore; ocean: fixed SST + Charnock drag)
Prognostic turbulent kinetic energy (TKE)
Shallow moist convection
Orographic gravity wave drag
Kuo convective scheme
Explicit condensation: large-scale supersaturation removal
Advanced radiative computation (solar + IR)

All experiments were performed with version 3.0 of the MC2 model (first distributed version in 1994) and with the very same physics configuration (Table 5) as the one used in the operational version of the RFE model. This physics configuration was also used to run the RFE model on all COMPARE I experiments. We did not use the proposed number nor positions of the vertical computational levels because of an earlier problem with the choice of the wavenumber scan strategy in the ADI pressure solver for the 3D Helmholtz equation, causing it not to converge accurately enough. The pressure solver was in fact unable to resolve the full spectrum of vertical waves imposed by the proposed σ-type vertical layering. We therefore opted for a more uniform distribution of vertical levels involving a constant stretching factor between two consecutive levels. Figure 10 shows the difference between the proposed distribution of vertical levels for experiment 2 (also used by the RFE model) and the one actually used by MC2. This problem with the pressure solver has since been corrected and it is now possible to use any reasonable vertical layering. A second set of MC2 runs with the improved ADI solver was made and submitted to the COMPARE evaluation committtee. Experiment 5 consisted of a self-nested 24-h forecast on domain B of Fig. 9 with lateral boundary and initial conditions extracted from experiment 4. All experiments were performed with a model lid at 30 km in order to include the very strong 10-hPa jet analyzed at 1200 UTC 6 March 1995 over northern Canada and southern Greenland.

2) RESULTS

Here we will concentrate on the 24-h forecast of experiment 5, feeling free to compare the results with those of other COMPARE participants as all have agreed to share their individual results. In general, the MC2 performance is relatively good and compares very closely to that of the RFE model since the two models were using the very same configuration of their common physics package. The two models predicted with good accuracy the secondary low southeast of Nova Scotia while overpredicting the primary inshore cyclone (Fig. 11). Both models also show a warm bias behind the continental system, while the position of the thermal ridge is in rather good agreement with the analysis (Fig. 11c). One can also notice the cold anticyclone over northeast Quebec, which is underdeveloped and forecast too far to the southeast.

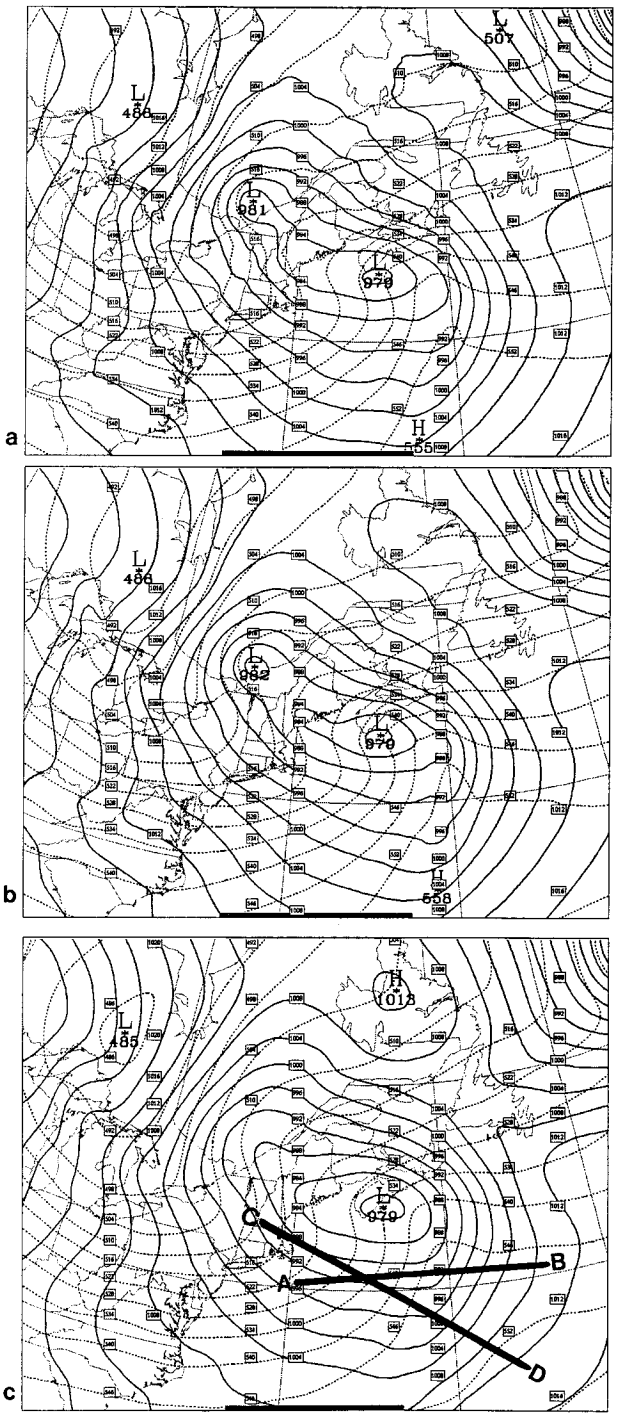

FIG. 11. (a) MC2 and (b) RFE 24-h forecasts corresponding to the (c) COMPARE 1 analysis valid at 1200 UTC 7 March 1986. Mean sea level pressure (solid) contoured every 4 hPa and 1000–500-hPa thickness (dashed) contoured every 6 dam.

A cross section through the cold front (Fig. 12) reveals the typical circulation associated with baroclinic

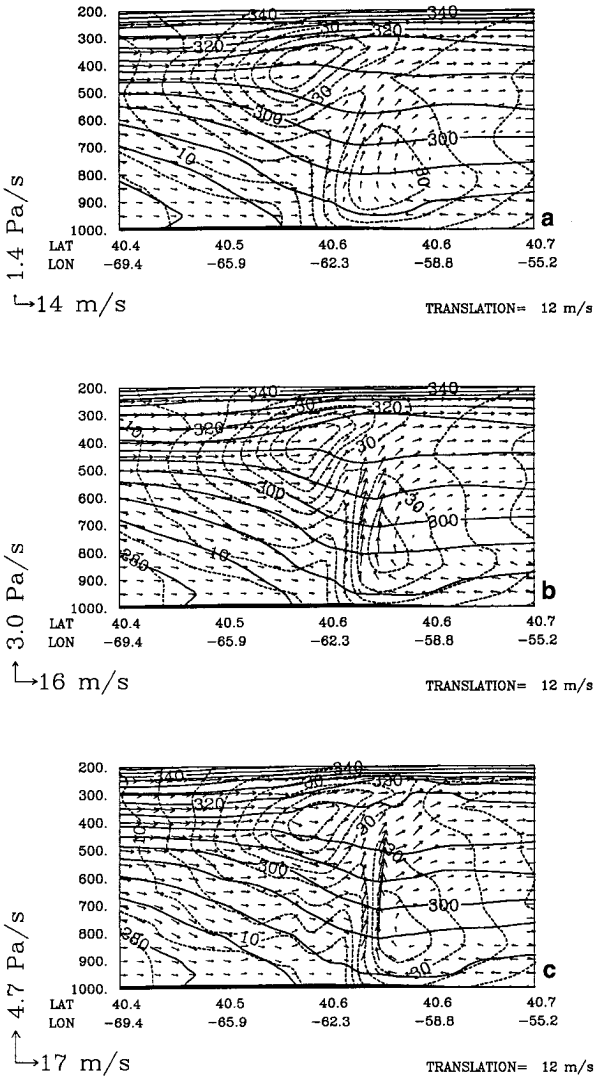

FIG. 12. Vertical cross section along baseline *AB* of Fig. 11c of the 24-h MC2 forecasts for (a) experiment 1, (b) experiment 3, and (c) experiment 5 of COMPARE 1. Potential temperature (solid) is contoured every 5 K and wind component (dashed) normal to the cross section is contoured every 5 m s^{-1}. Vectors denote velocity and vertical motion tangent to the cross section with scales indicated at lower left and a translation speed (at lower right) removed from the tangent flow.

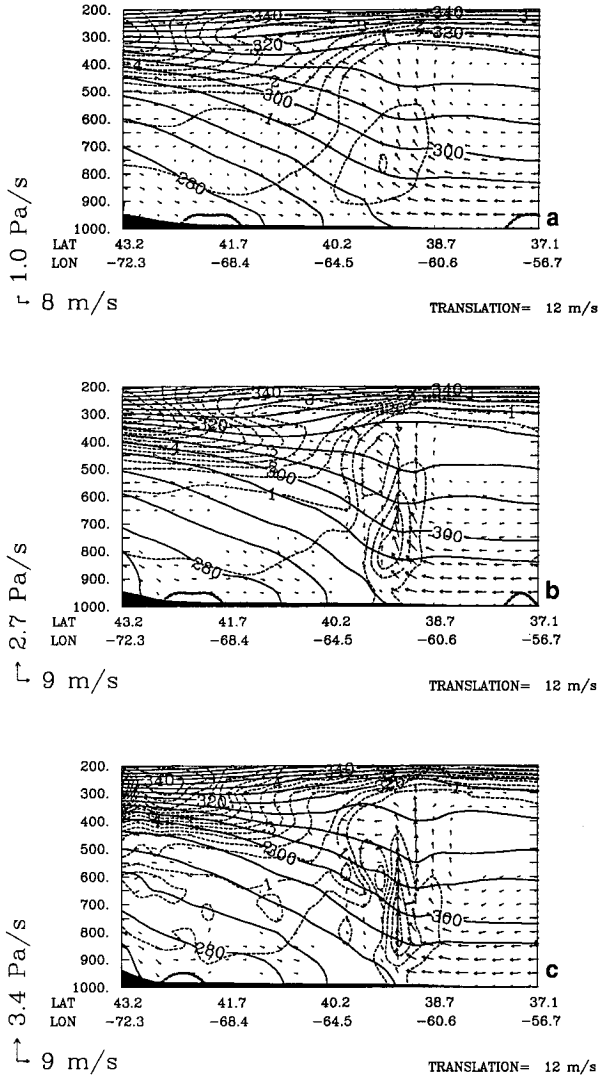

FIG. 13. As in Fig. 12, but for potential vorticity (dashed) contoured every 0.5 × 10^{-5} K hPa^{-1} s^{-1} and potential temperature (solid) contoured every 5 K. Vertical cross section is taken along baseline *CD* of Fig. 11c.

cyclogenesis. The main features of this circulation are very much in agreement with that of the analysis (Chouinard et al. 1994) even though the intensity of the vertical motion over the surface front along with the upper jet and LLJ are a bit stronger in the MC2 model. It is interesting to see the progression of the main forecast features as resolution increases. In particular, vertical motion more than triples in strength (reaching values of 4.7 Pa s^{-1}) and becomes much more horizontally confined when going from 100 to 25 km in horizontal resolution. However, the strength of the lower- and upper-level jets only intensifies when going from 100 to 50 km. Smaller perturbations behind the cold front are also worth noticing, especially in the upward vertical motion, which does not show up in the analysis but can clearly be associated with the cloud structure seen on the satellite image (Stewart et al. 1987). The potential vorticity cross section of Fig. 13 is also very much in agreement with the analysis but reveals more clearly the potential vorticity (PV) anomaly, associated with the tropopause fold, which overruns the low-level baroclinic zone. This result is consistent with that of Hoskins et al. (1985), who suggested that such a feature is typically associated with surface cyclogenesis. Potential vorticity over the surface front increases drastically with resolution as static instability becomes more intense and more confined horizontally.

Standard scores for both the MC2 and RFE models were computed for experiment 5 (Fig. 14). Twenty-four-

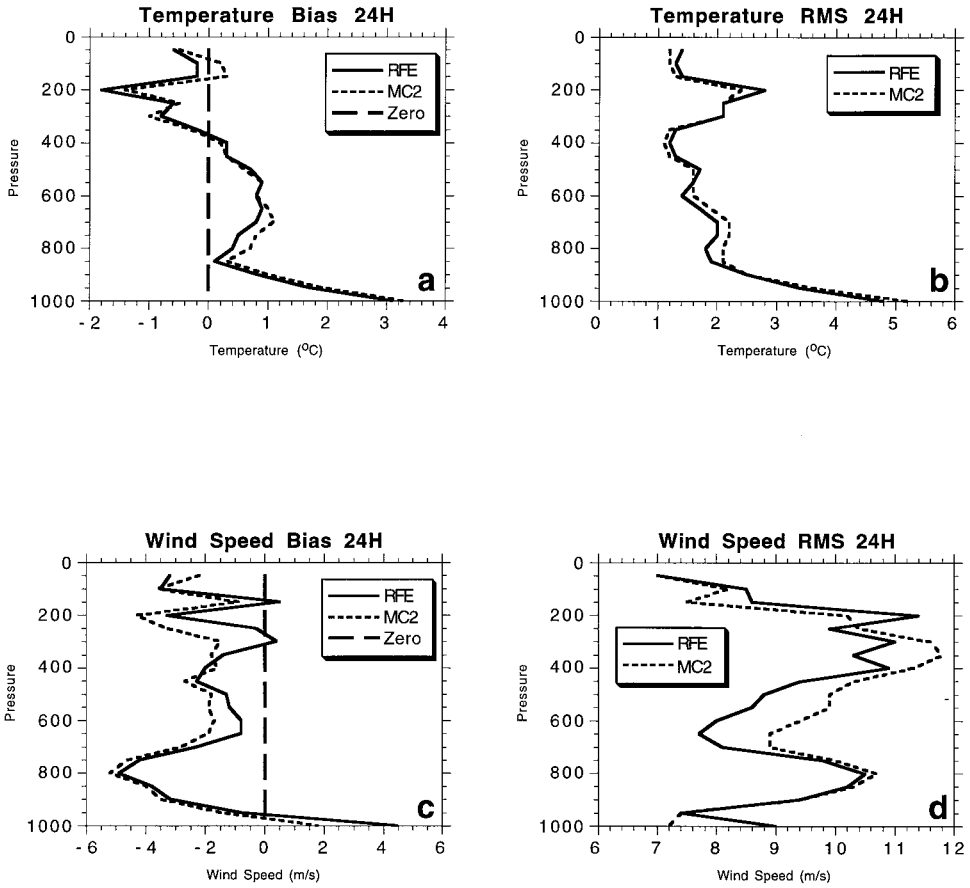

FIG. 14. Standard scores for both the MC2 and RFE models for experiment 5 (24-h forecasts) of COMPARE 1: temperature (a) mean and (b) rms error; wind speed (c) mean and (d) rms error.

hour temperature and wind speed forecasts were compared to the analysis of 1200 UTC 7 March 1986 over the COMPARE 1 verification domain (domain C of Fig. 9). Results for the two models are in general very similar, especially in the temperature forecast where the largest error can be observed near the surface (rms error near 5°C). The errors associated with the wind speed forecast are a bit more different as the MC2 model shows a stronger negative bias than the RFE model in the upper levels. Near the surface, however, the RFE shows a much stronger positive bias (4.5 m s^{-1}) than MC2 (1.5 m s^{-1}); this also appears in the 1000-hPa rms errors, with 9 m s^{-1} for the RFE and 7.2 m s^{-1} for the MC2. It is suggested that this difference be attributed to the fact that the MC2 model does not use the physics ''tendencies'' computed by the SLD routine [see section 3b(2)] for the horizontal components of the wind on the first thermodynamic level. The SLD seems, in this particular case study, to overestimate the surface wind, especially in regions where the surface fluxes are important, that is, an unstable surface layer. The cross section of Fig. 15 gives a clear example of the kind of surface decoupling produced by the SLD under certain conditions ocurring in several cases studied with MC2 but that we have not attempted to characterize.

In an attempt to measure the nonhydrostatic effects associated with this rapid oceanic cyclogenesis, experiment 5 has been performed a second time using the MC2 model in its hydrostatic mode. This particular mode of operation can easily be selected externally by the user as part of the run-time model configuration. The hydrostatic mode is achieved by setting $\delta_h = 0$ in Eq. (2.3). Small differences were observed in the 24-h forecast, especially in the warm sector. Those differences mainly consist of very small-scale phase errors (one to two grid points) and do not affect the overall forecast in any significant way. Root-mean-square differences between the 24-h forecasts were computed on 20 levels for u, v, w, T, and q (Table 6) over a horizontal domain covering a little more than the warm sector itself (where differences were observed). Those rms differences are very small and confirm the absence of significant nonhydrostatic effects in a 25-km resolution run. This result was in fact predictable and is consistent with the suggested horizontal resolution threshold of 9.5 km (Bubnova et al. 1995) or 8-km wavelength (Daley

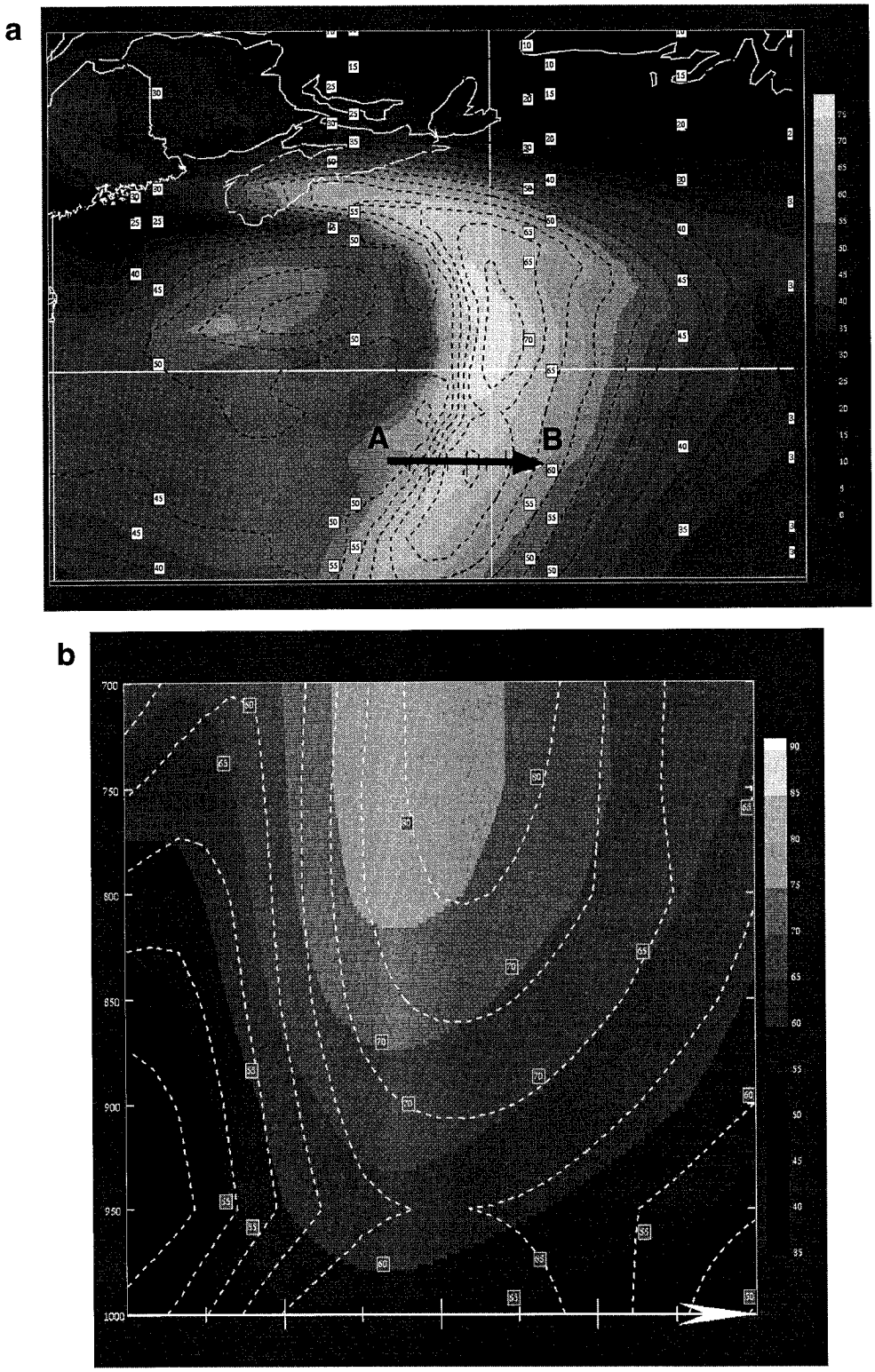

FIG. 15. (a) MC2 (shaded) and RFE (dashed black) 24-h forecasts (experiment 5) of the warm sector LLJ at 850 hPa. Wind module is contoured every 5 kt. (b) Cross section taken along baseline *AB* of (a) over the 1000–700-hPa layer; RFE is dashed white.

TABLE 6. Root-mean-square differences between hydrostatic and nonhydrostatic 24-h forecast (experiment 5, COMPARE 1).

	Max rms difference	Level (hPa)	Typical field values
u (kt)	0.190	300	90.0
v (kt)	0.160	300	100.0
w (Pa s^{-1})	0.031	650	40.0
T (°C)	0.031	700	−30.0
q (10^{-3})	0.025	800	8.0

1988) beyond which nonhydrostatic effects may become important.

The following example provides a much deeper test of our nonhydrostatic model.

b. Downslope windstorm over Cape Breton Island

Atmospheric responses to a disturbance created when stably stratified air is forced to rise over a topographic barrier are of many types. Among the well-documented responses are the downslope windstorm events most often observed on the lee side of major mountain ranges such as the Rockies, the Alps, and the Pyrénées, where they sometimes become severe. However, they also surprisingly occur for much shallower mountain ridges such as the Cape Breton Highlands in Nova Scotia.

Different mechanisms to explain these severe events have been proposed over the years, for example, the older hydraulic theory (Long 1954; Smith 1985; Durran 1986), the vertically propagating wave theory (Klemp and Lilly 1975), and the resonant or breaking wave theory (Clark and Peltier 1977; Laprise and Peltier 1989a,b). However, these theories often deal with breaking wave flows generated by major mountain ridges. A linear, analytic, and two-dimensional study was first performed by Queney (1948). Long (1953) resolved the nonlinear problem, revealing certain cases of nonbreaking wave flows associated with downslope windstorms. Finally, in two-dimensional flow studies, Stein (1992) with the PERIDOT model (Imbard et al. 1987) and Pinty et al. (1995) with the MC2 model investigated different airflow regimes for classic orographic problems. A slight enhancement of the surface drag, resulting in a downslope acceleration on the lee side of the mountain is observed with linear to weakly nonlinear airflow regimes. This slight increase in the surface drag generates a pattern analogous to the one resulting from a transition from subcritical to supercritical flow in the hydraulic theory (hydraulic jump). As suggested by Durran (1990), there appears to be three different circumstances in which the atmospheric response is analogous to an hydraulic jump: 1) wave breaking (Clark and Peltier 1977), 2) Scorer parameter layering (Durran 1986), and 3) capping by a mean-state critical layer (Smith 1985).

The MC2 model was used to simulate the downslope wind event of 21–22 December 1993 on the western lee side of the Cape Breton Highlands, Nova Scotia. This particular type of wind event, locally called ''suete'' (an Acadian term meaning southeast), regularly occurs when strong winds develop from the southeast. At 1200 UTC 21 December, a low pressure system at 992 hPa

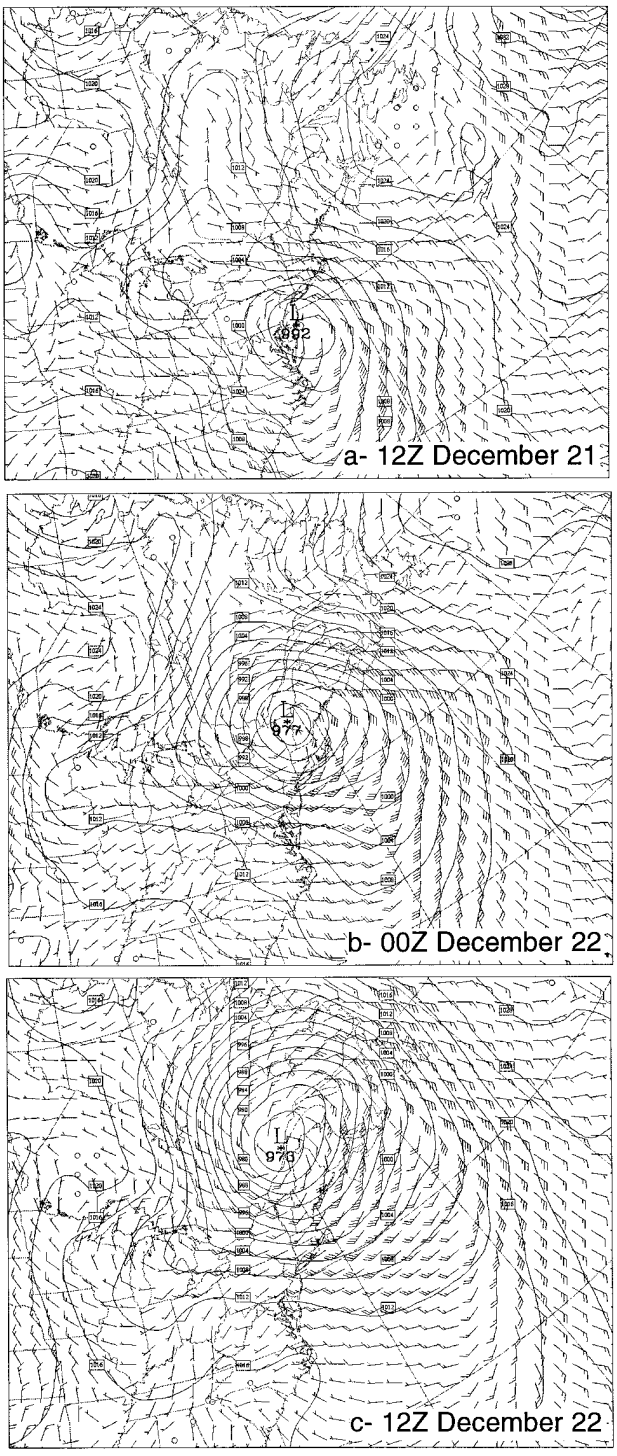

FIG. 16. CMC analysis for (a) 1200 UTC 21 December, (b) 0000 UTC 22 December, and (c) 1200 UTC 22 December 1993. Mean sea level pressure is contoured every 4 hPa. Wind barbs are in knots.

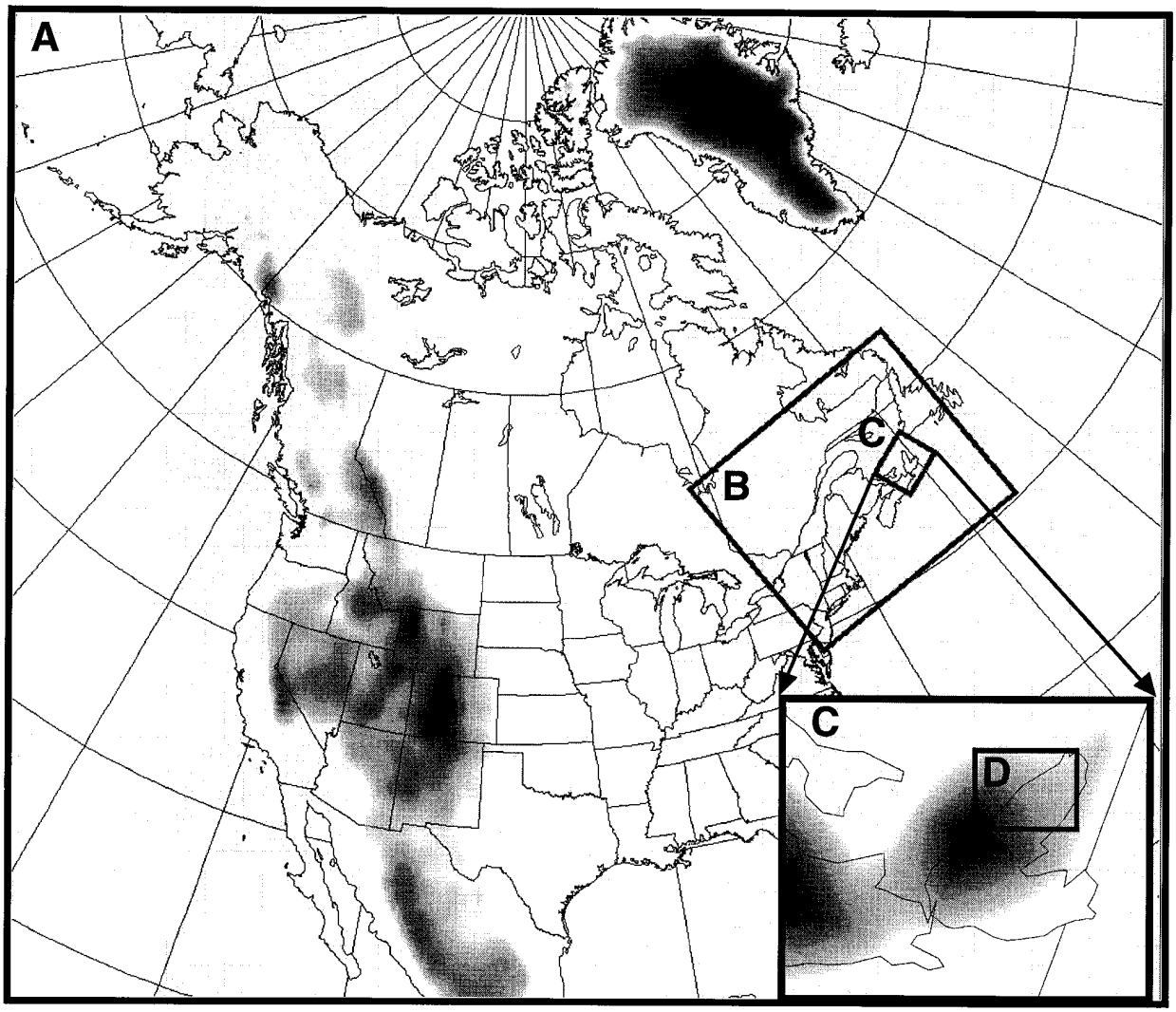

FIG. 17. Grid strategy for the simulation of the suete event of 21–22 December 1993. Four cascaded grids are used, covering windows A, B, C, D; specifications are given in Table 7. Shading is 50-km terrain.

was developing and moving northeastward from the Delaware Bay region (Fig. 16a). By 0000 UTC 22 December (Fig. 16b), the system had moved to northern Vermont with a quite intense cold front extending to the south. Strong southeasterly winds had then developed in the warm sector and led to the onset of the suete phenomenon. Note that the suete itself is a result of an early orographic wave that speeds up the formation of an intense wind core in the lee of the mountain ridge, before the very strong synoptic winds invade the whole region. The suete was observed from 2000 UTC 21 December to 0900 UTC 22 December by an automatic station (CWZQ) located at Grand Etang near Cheticamp (Fig. 18). Winds of up to 45 kt gusting to 60 kt were recorded for a few hours after 2300 UTC 21 December (Fig. 21). After about 0600 UTC, the cold front swept across Nova Scotia and winds shifted to the southwest (Fig. 16c), thereby ending the suete phenomenon.

1) METHODOLOGY

The grid strategy used for this simulation is very similar to the one used by Jackson and Steyn (1994) in a fjord gap wind simulation (Howe Sound, British Columbia) using the CSU RAMS model. For our suete simulation, the model was run on four consecutive one-way nested grids using the cascade technique described in section 4. Horizontal resolution was here brought from 50 km down to 400 m in order to better resolve the topographic forcing. The four grids are depicted in Fig. 17 and are fully described in Table 7. The first three runs (Fig. 17, grids A, B, C) were performed using the same physics configuration as for the COMPARE 1 case (see Table 5). The same 25 computational levels were used for those three runs. The first thermodynamic level was set at 80 m and a constant stretching factor of about 1.15 was applied on each successive layer to span a

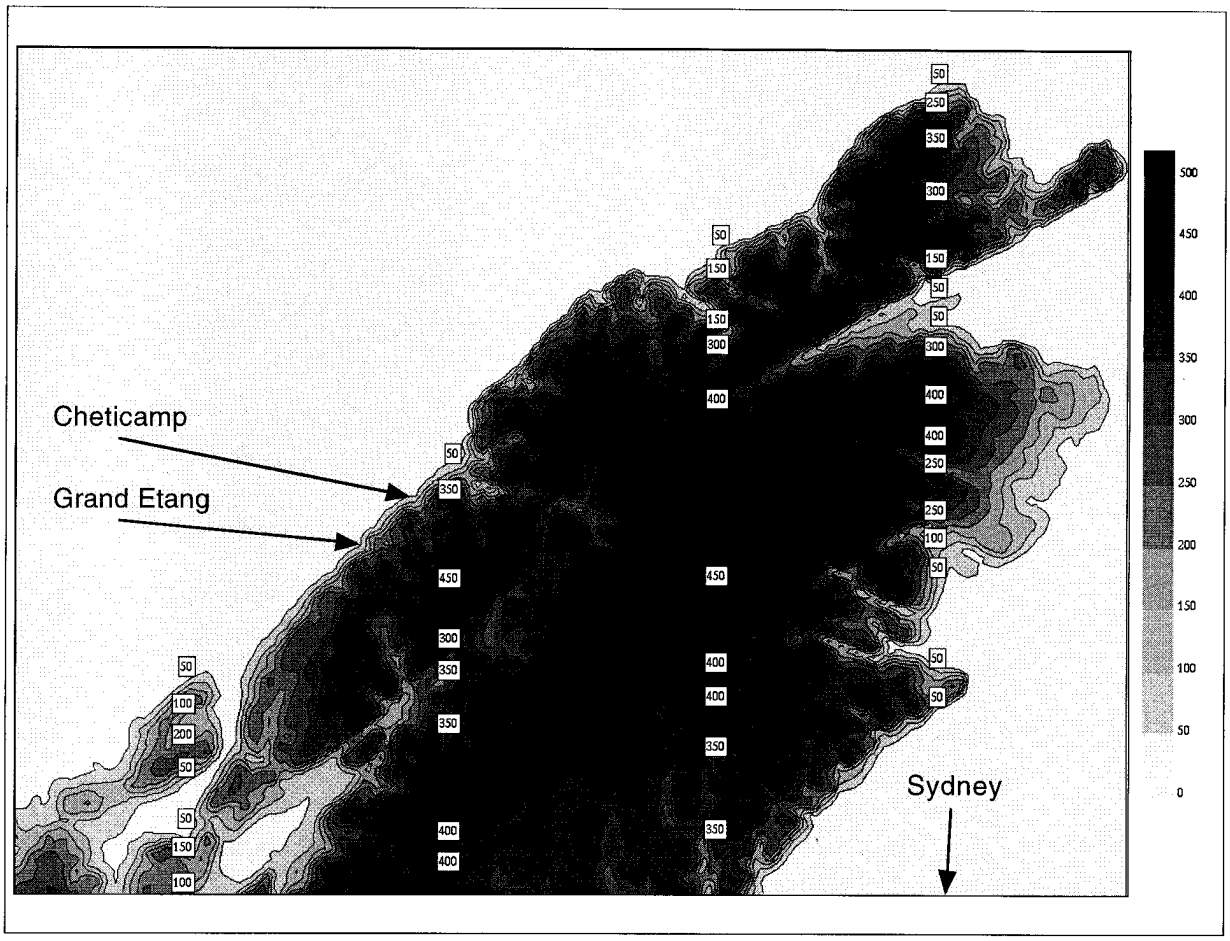

FIG. 18. The 500-m resolution topography over northern portion of Cape Breton, Nova Scotia. Interval of 50 m.

vertical domain of 30 000 m. No vertical nesting was performed in the first three runs.

The last run (400-m resolution) (Fig. 17, grid D) was performed without radiative calculation, convective scheme, nor gravity wave drag. Vertical layering was achieved again on 25 levels except with a first thermodynamic level set lower at 30 m. A stretching of about 1.17 was used to cover a vertical domain of 15 000 m thus focusing somewhat the vertical resolution in the PBL. Vertical nesting was here performed on the topmost 5000 m below the model lid in order to minimize upper boundary effects. This 400-m resolution matches the maximum resolution of our current topography database (DEM), that is, 500 m.

The 50-km run was initialized with the CMC 50-km regional analysis of 0000 UTC 21 December and the three subsequent analyses at 12-h interval were used to provide the lateral boundary conditions. That first run was simply used to capture the synoptic conditions over a period of 36 h for the next cascade runs and will not be discussed further. The starting point of the 10-km run is the 12-h forecast of the 50-km domain and is integrated for 24 h using an 18-km resolution DEM. The starting point of the 2-km run is the 9-h forecast of the 10-km domain and is run for 7 h. Finally, the starting point of the 400-m run is the 5-h forecast of the 2-km domain and is run for 1 h. Note that this gradual time shift of the start time for the higher resolution runs, which corresponds generally with the widely practiced technique of preforecasting, ensures that the lateral boundary and initial conditions have gone through a spinup period to adjust with the resolution of the parent grid. The last two runs were performed using a very high resolution DEM (500 m) on which a special Cressman-type filter is applied as an averaging operator acting on each of the two target grids. Figure 18 shows the topography used for the 400-m run.

2) RESULTS

The time evolution of the surface wind patterns from the 10-km run clearly shows the onset of the suete event, on the lee side of Cape Breton, between 1800 UTC 21 December and 0000 UTC 22 December (Fig. 19). A narrow near-surface jet then strengthens just off the west

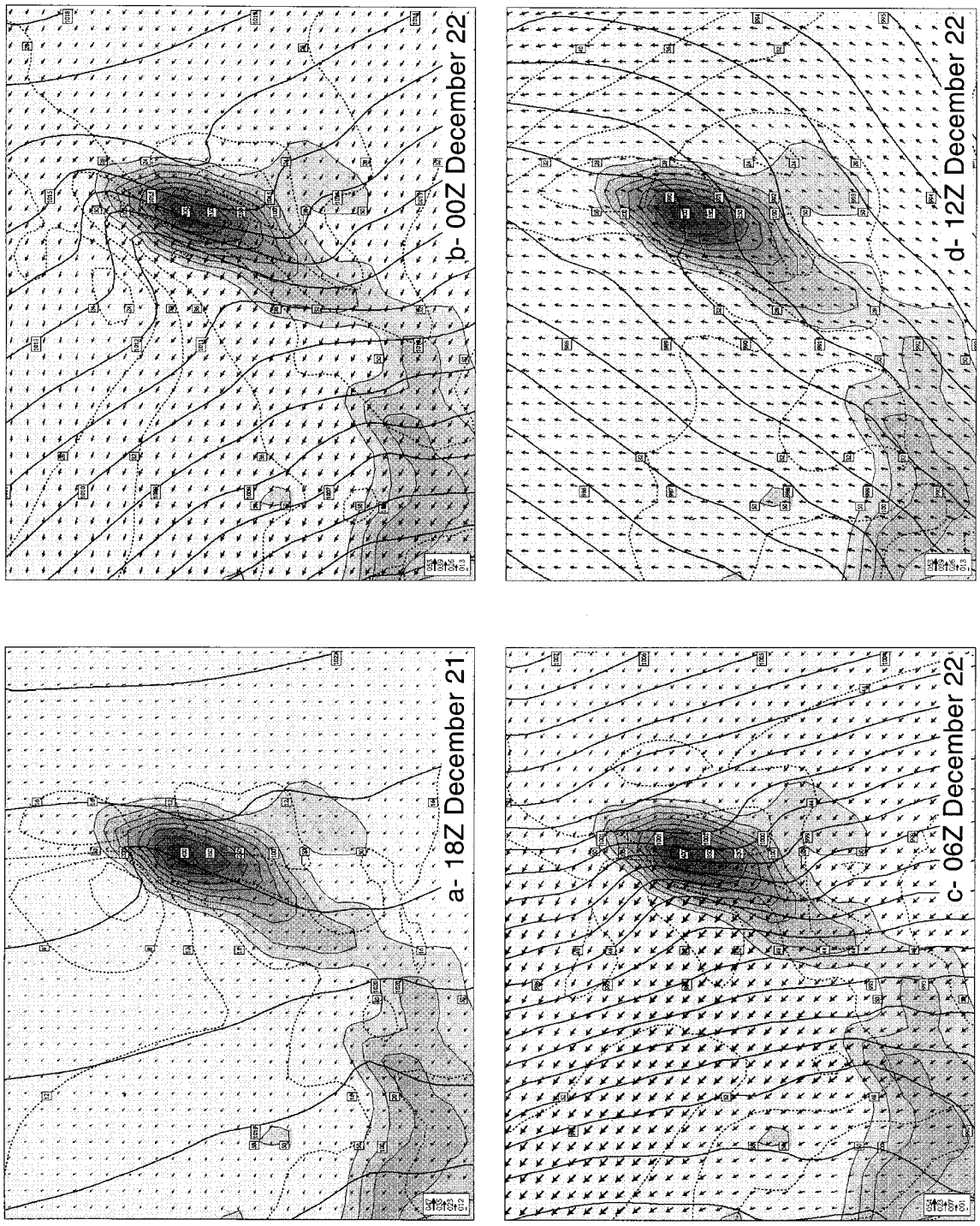

FIG. 19. MC2 10-km forecast after (a) 6 h, (b) 12 h, (c) 18 h, and (d) 24 h for the suete of December 1993. Shades of gray represent the 10-km topography (contoured every 50 m). Mean sea level pressure (solid) is contoured every 1 hPa and 10-m wind module (dashed) is contoured every 4 kt. Vectors denote 10-m horizontal flow with scale indicated on lower left corner.

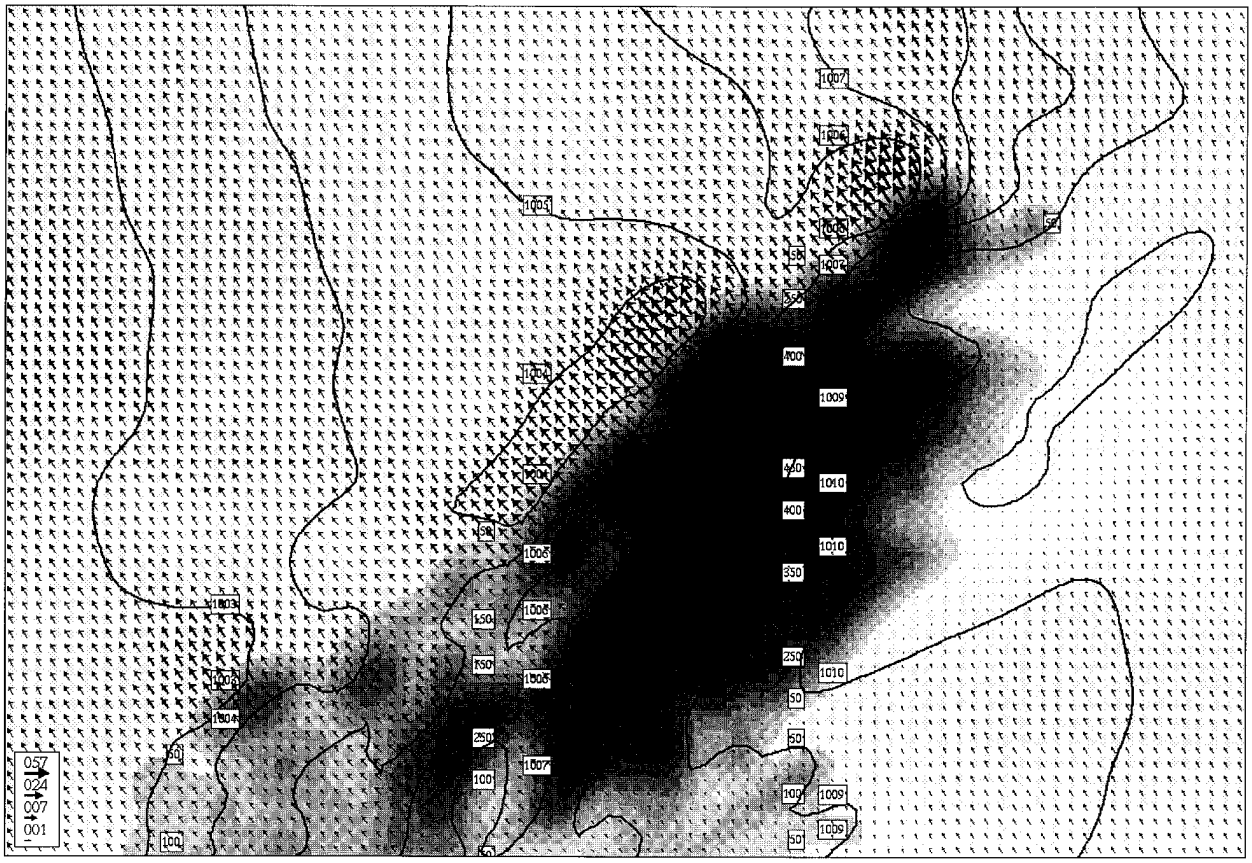

FIG. 20. MC2 2-km 6-h forecast valid at 0300 UTC 22 December 1993. Mean sea level pressure (solid) is contoured every 1 hPa. Vectors denote 10-m horizontal flow with scale (kt) indicated on lower left corner. Shades of gray represent the 2-km topography (with a 50-m shading increment).

coast, reaching a maximum of 55 kt by 0600 UTC (Fig. 19). At this stage the strong synoptic winds have already begun to invade the domain, and the suete is not so well defined. The overall wind structure thereafter changes drastically as synoptic winds become southwestward (Fig. 19), hence ending the suete event. Of some interest is the mesoscale trough developing on the lee side of the mountain crest along with the ridge that builds up on the windward side. This pressure dipole (here 4 hPa) is a typical surface signature of the presence of a mountain wave.

The suete event is captured with much more detail in the 2-km run where the maximum surface winds are forecast on an even narrower band closer to the coast (Fig. 20). Two regions of strong downslope winds can be observed. One is located near Cheticamp and the other one near the northern end of the highlands. The suete is shown here to have an offshore near-surface extension of about 20–25 km with the strongest winds located within 10 km of the shore. When compared against the observations, it can be seen that for the station on the lee side of the mountain (Grand Etang, Fig. 21), the accuracy of the surface wind forecast increases significantly with the resolution, whereas for the station on the windward side (Sydney, Fig. 21), the resolution has practically no effect on the accuracy of the forecast. This is consistent with the fact that high resolution is needed to capture properly the mesoscale topography effect on the lee side, whereas a much coarser resolution is sufficient to forecast the synoptic conditions on the upstream side far enough from the mountain.

The low-level (900 hPa) vertical velocity of the 2-km run displays two types of elongated cells mutually perpendicular (Fig. 22a): stronger ones that are perpendicular and close to the lee side slope and weaker ones that are parallel to the exit flow. Figure 22b shows a cross section, along baseline *AB* of Fig. 22a, of the vertical velocity over Cape Breton where a weak downstream vertical tilt of the main mountain wave can be observed by drawing an imaginary straight line between the $+220 \times 10^{-1}$ Pa s^{-1} low-level subsidence and the -40×10^{-1} Pa s^{-1} ascent above it, at 700 hPa, and to the right. This is a clear indication that relatively small nonhydrostatic effects are present in this 2-km solution (Pinty et al. 1995). Taking an average value of 0.015 s^{-1} for the Brunt–Väisälä frequency (N), 15 km for the half-width of the mountain (L), and 15 m s^{-1} for the mean horizontal velocity (U) over Cape Breton at 0900 UTC, the

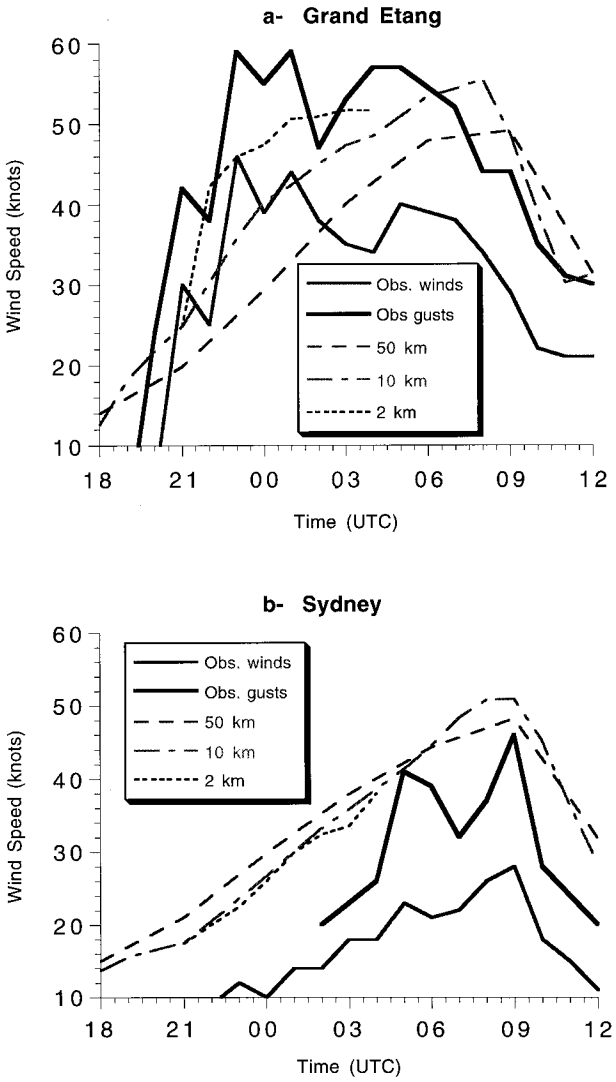

FIG. 21. MC2 50-, 10-, and 2-km forecasts against the observations for the suete event of 21–22 December 1993 for (a) downstream (Grand Etang) and (b) upstream (Sydney) stations. The stations are indicated in Fig. 18.

nondimensional mountain half-width number NL/U reaches a value of only 15. Low values of this number are normally associated with nonhydrostatic flows. On the other hand, taking 500 m as the height of the mountain (h), the inverse Froude number Nh/U gives a value of 0.5 that classifies this mountain wave as weakly nonlinear (Pierrehumbert and Wyman 1985). The vertical extent of the wave seems here limited by the presence of a critical level near 5 km above sea level (ASL) where the horizontal flow is at a 90° angle to the right of the near surface flow (see Fig. 24). The wave seems therefore trapped below 500 hPa (Fig. 22b) and can be seen to propagate downstream to a distance of about 50 km. This wave propagation takes here the form of elongated plumes of vertical motion extending off the whole length of the west coast. The fine details in the horizontal

TABLE 7. Grid strategy for the suete case.

Grid	Δx (km)	ni × nj	Δt (s)	Start date	Forecast (h)
1	50	181 × 155	720	0000 UTC 21 Dec	36
2	10	191 × 161	180	1200 UTC 21 Dec	24
3	2	171 × 141	30	2100 UTC 21 Dec	07
4	0.4	199 × 151	6	0200 UTC 22 Dec	01

(Fig. 22a) and vertical (Fig. 22c) structure of those plumes have been verified to match closely with the details in the topography.

A subsequent 2-km hydrostatic run was also performed in order to more formally assess the nonhydrostatic effects. For this purpose, we focus on the hydrostatic vertical motion and choose to display it (Fig. 23) in the same manner as in the preceding Fig. 22. Although the hydrostatic solution appears similar in nature, the vertical motion associated with the mountain wave is much stronger (-60×10^{-1} Pa s^{-1} ascent at 700 hPa) and the downstream tilt of the main wave is much smaller than in the nonhydrostatic solution (Fig. 23b). It is also worth noticing that, in this mode, the waves do not propagate downstream from the west coast much farther than about 10 km (Fig. 23a) and that the vertical structure is less trapped below the critical level. The vertical structure of the propagating plumes of vertical motion (Fig. 23c) is also much weaker and far less organized than in the nonhydrostatic solution.

In hydraulic theory, the Froude number is often defined as $\mathrm{Fr} = u^2/c^2$ where u is the mean fluid velocity and $c = gh\Delta\rho/\rho_0$ (with g as gravity, h as thickness of the lower fluid layer, and ρ as density), sometimes referred to as the reduced gravity for a two-layer fluid. As an upstream subcritical flow ($\mathrm{Fr} < 1$) ascends the upslope side of an obstacle, Fr tends to increase both from the increase in u and the decrease in c. If Fr reaches 1 at the crest, the flow then becomes supercritical and accelerates very rapidly as it descends the barrier. The adjustment back to subcritical conditions normally takes place in what is known as a turbulent hydraulic jump (Durran 1986, 1990; Holton 1992). Referring now to Fig. 24, one can easily observe two distinct layers in the flow going over the mountain. One at a low level, bounded above by the 290-K isentrope, and the other one higher above, associated for convenience with isentrope 298 K. The low-level flow is much more disrupted than the higher level one as it crosses over the mountain. Isentropic surfaces are in fact bunching up together on the lee side and, in the region immediately following the strong downward vertical motion, a glimpse of a hydraulic jump can be observed as the vertical gradient of potential temperature adjusts itself back to its windward state. Taking h as the height of the 298-K isentropic surface and using appropriate densities for the two layers defined above, the Froude number was computed for the 6-h forecast of the 2-km run

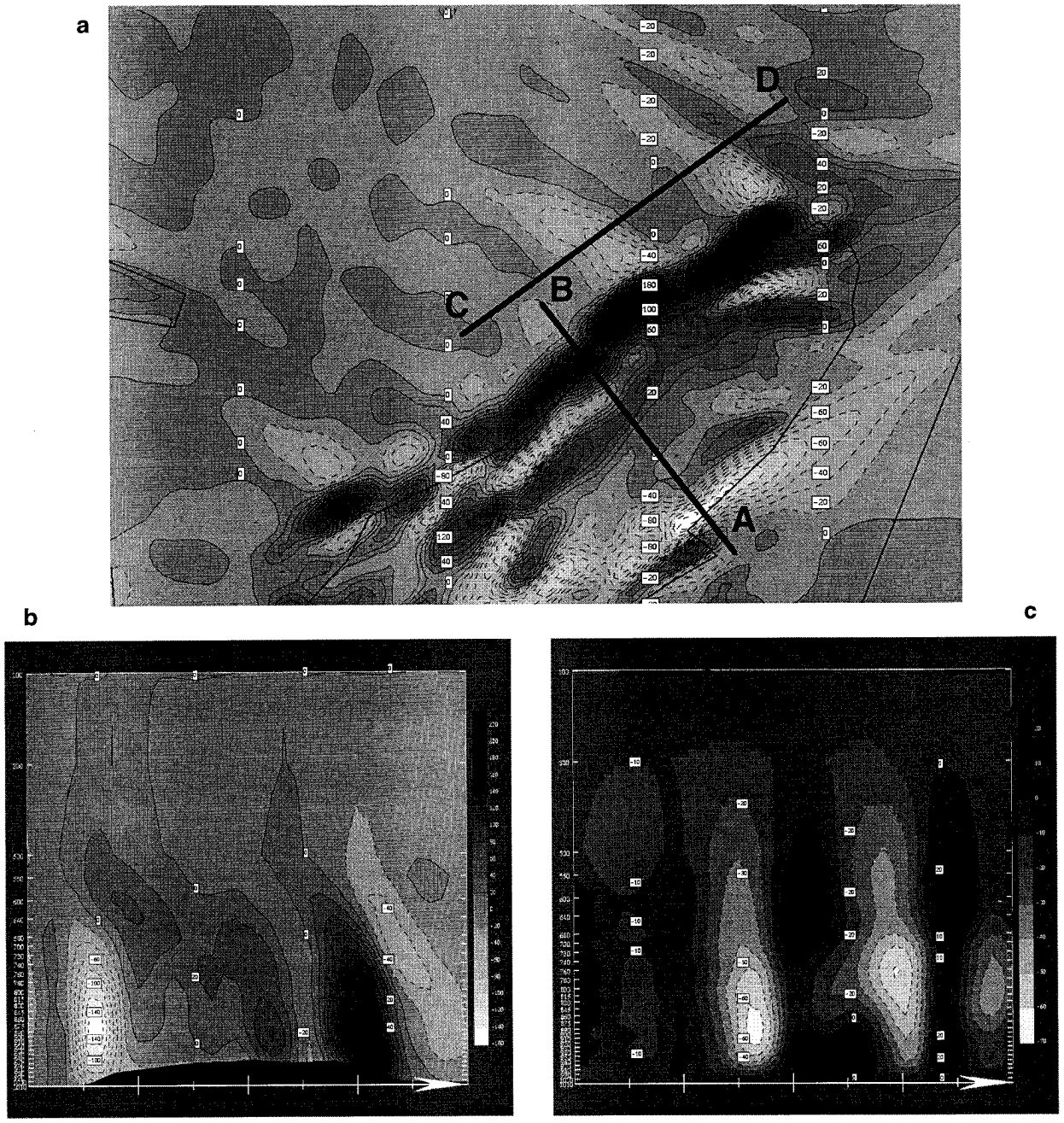

FIG. 22. (a) The 6-h forecast of the 900-hPa vertical motion, valid at 0400 UTC 22 December 1993, from the 2-km nonhydrostatic run. (b) A vertical cross section taken along baseline *AB* of (a). (c) A vertical cross section taken along baseline *CD* of (a). Vertical motion is contoured every 20 Pa s^{-1} for (a) and (b) and every 10 Pa s^{-1} for (c); dashed for negative (i.e., upward) values. Top of cross sections is the 100-hPa level; terrain silhouette appears therein.

(Fig. 25). Although a bit too large, 1.1 in the far-field outflow, the Froude number distribution around the mountain for this suete event shows a remarkable consistency with the hydraulic theory as a maximum value of 1.5 is reached on the lee side of the mountain and the critical value of 1 coincides well with the crest line of the plateau. From its maximum of 1.5, Fr then relaxes toward lesser values near 1.0 over a relatively small distance, which can be associated with the hydraulic jump. Horizontal winds decrease by about 20 kt within the jump. This strong gradient in the strength of the surface winds constitutes a definite hazard for navigation and may in fact be responsible for some of the shipwrecks that occured during past suete events. The Froude number analysis presented here compares rather well with the one of Jackson and Steyn (1994) in the

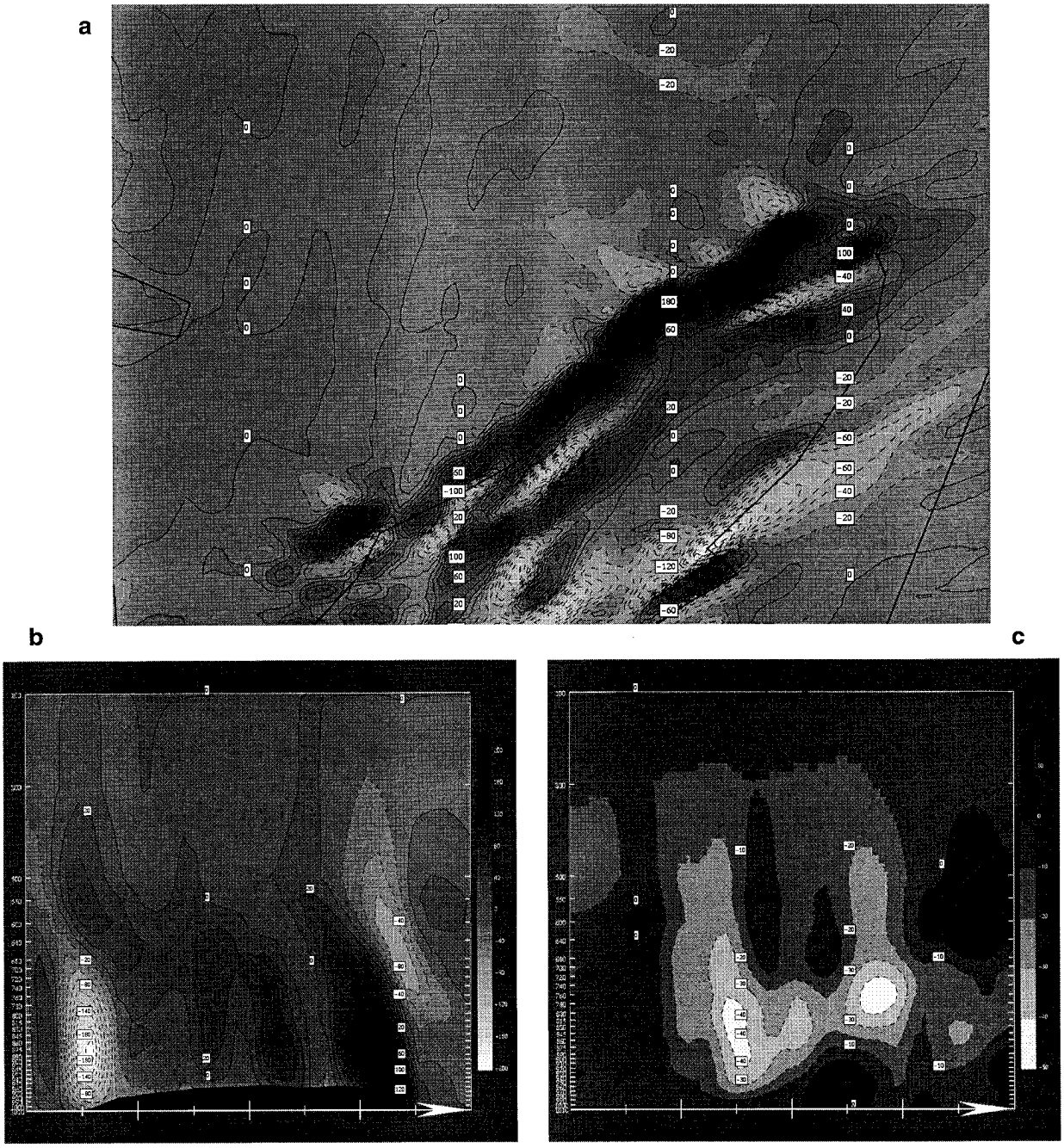

FIG. 23. As in Fig. 22 except that vertical motion is from the 2-km hydrostatic run.

above-mentioned fjord gap winds simulation with the CSU RAMS model.

The 0.4-km run does not offer much more information than the 2-km run, although the flow *adapts* itself very accurately to the high resolution topography (Fig. 25). From the terrain silhouette also shown in Fig. 26, one can appreciate the plateau shape and the very sharp slopes at the two ends. The western ''cliff,'' on the right, has a slope of about 1:5, that is, 11°. This last run improves the definition of the hydraulic jump. Finally, when looking at the Froude number of Fig. 26, one can observe a new feature in the form of an elongated tongue of high Froude number downstream from the 1.7 maximum near the coast. The main purpose of the 0.4-km run was in fact to test the model's self-nesting capability and the vertical nesting. It is also the first time that MC2 achieves a quasi-isotropic 3D mesh at about 500-m resolution in all three directions. Better results at very high resolution will only be possible with higher-resolution analyses and physics

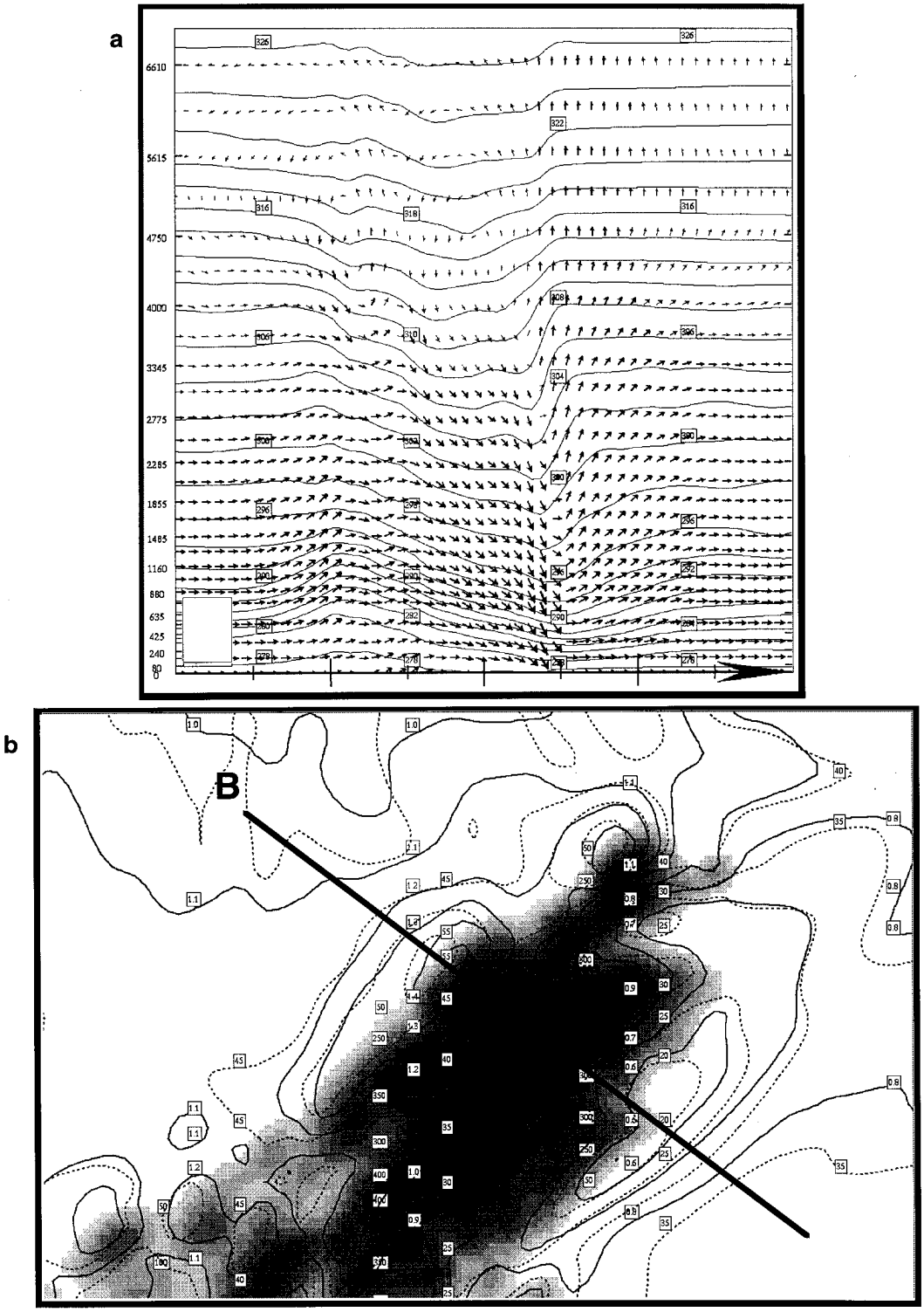

FIG. 24. The 6-h forecast from the 2-km run valid at 0300 UTC 22 December 1993. (a) Isentropic cross section, in Gal-Chen coordinates, along baseline *AB* of (b). Top of cross section is near 6000 m. Potential temperature contoured every 2 K. Vectors represent the in-plane flow. (b) Froude number (solid) contoured every 0.1 and 10-m wind module (dashed) contoured every 5 kt. Shades of gray represent the 2-km topography.

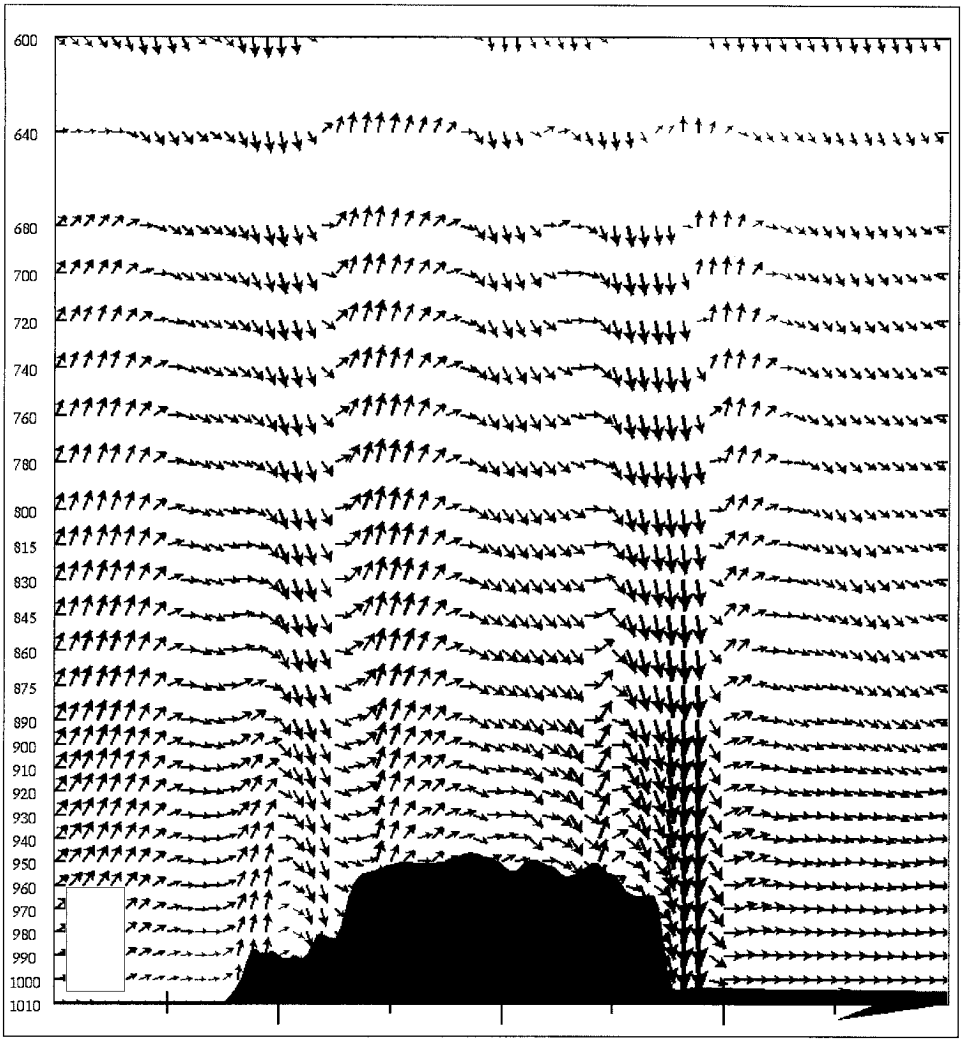

FIG. 25. Cross section, in isobaric coordinates, along baseline *AB* of Fig. 26b. Vectors represent the in-plane flow for the 1-h forecast of the 400-m run valid at 0300 UTC 22 December 1993. Terrain silhouette is included. Top at 600 hPa.

better adapted for this extremely fine (by NWP standards) horizontal resolution.

6. Summary and perspective

A rather long time has elapsed in the writing of this paper since MC2 was first made available, indicative of the numerous mesoscale applications (and the required support) for which it was immediately considered to be interesting. This rapid increase indicates a large previously unsatisfied need for mesoscale model products in Canada.

We have summarized the semi-implicit semi-Lagrangian (SISL) dynamics of the model and then emphasized more fully the interfacing with a comprehensive physics package, particularly the passage from Gal-Chen to sigma vertical coordinate, as well as the handling of wind in the lowermost layer. Concerning nesting and initialization, the nesting weights were documented, the usefulness of a simple forward–backward sequence of dynamical steps was demonstrated, and we presented preliminary results showing that MC2 could be used as a stand-alone forecast model.

The first application of the model discussed in detail here was the COMPARE 1 cyclogenesis case. We have established that the model was equal in meteorological performance to a well-established operational model, at the meso-α scale (i.e., runs at resolutions not exceeding 25 km). We confirmed the absence of nonhydrostatic effects at these coarse resolutions.

The second application was a local downslope windstorm phenomena (suete winds). It permitted us to demonstrate the high-resolution modeling potential of MC2 by solving a problem on large grids reaching resolutions exceeding 1 km and thus well into the meso-γ nonhydrostatic range. Here again the performance was ex-

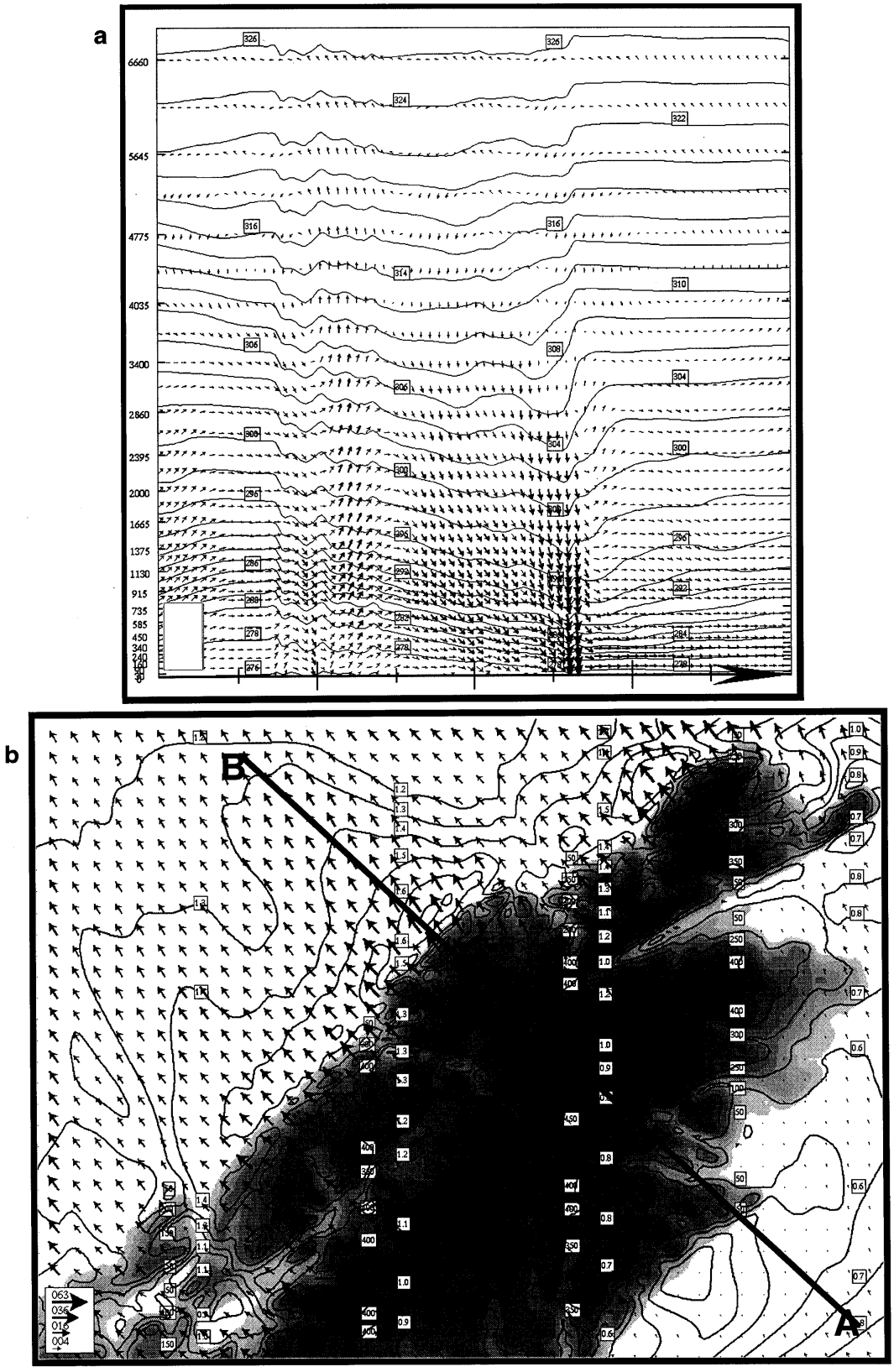

FIG. 26. As in Fig 24 except for the 1-h forecast of the 400-m run. Shades of gray represent the 400-m topography.

cellent and shown to yield features similar to those of other currently available mesoscale models but having more traditional numerics for their dynamics.

Much remains to be done to develop the potential of MC2 fully. What is probably the deepest deficiency is the current lack of a mesoscale data assimilation capacity able to absorb all currently available conventional meteorological observations: this will open the door to the simulation of mesoscale transient features. Exploratory work has begun along the lines of the incremental approach of Courtier et al. (1994) joined with the 3D variational method. Highly important from the numerical perspective is the introduction of *optional* Eulerian advection to further investigate the claim of P. Bartello and S. Thomas (personal communication, 1997) that the semi-Lagrangian approach becomes inefficient at the finest mesoscales and ''the need for a complete reevaluation of the method before application to mesoscale and small-scale forecasting.'' Indeed, the initial demonstration by TRL was not definitive since it used a 127-km grid resolution.

On the computer science side, a simplified porting of the kernel of MC2 to a massively parallel processor architecture (both distributed and shared memory) is being examined.

An appealing area for MC2's capacities is the direct support for the improvement of larger-scale parametrizations. It can take the form of direct very fine-scale simulation and areal budgeting to validate proposed parametrizations, such as the new orographic drag parametrization of Lott and Miller (1994). Or, also, identifying and removing the mean long-term error profiles due to a given complete physics package; to that end, the technique of running an LAM over a 1-month period with perfect lateral BCs, as used by Sass and Christensen (1995), appears very efficient. Also, the advanced type of interfacing with the model dynamics and the special conditions for instance with the diabatic term in our form of the continuity equation allow to investigate for an optimum coupling of the physics feedbacks, especially in terms of heat and mass fluxes. In doing so, MC2 will contribute to the development of new physical schemes at RPN.

Of course the incipient and future major applications of this model will be in the air quality, agrometeorological, and short-term water management domains. These are quite distinct from current major goals of NWP centers. Also, the question of applying MC2 in CMC's operations is still unclear as of now. The quality and efficiency of MC2 have to be examined more carefully by mesoscale NWP standards and, in the case of CMC, weighted against the variable mesh technique on which its current (and future contemplated, i.e., GEF) mesoscale models are based.

Acknowledgments. In the first place and above all, we express our profound respect to the genius and far-reaching view of deceased Emeritus Scientist Professor André Robert: without his talent and his final dedication to so many graduate students at UQAM, the MC2 would not have been born. We also place a great importance on our relationship with the research team at UQAM under the leadership of Prof. René Laprise, who shares with us the benefits of their more basic modeling research. We also thank the Cooperative Centre for Research in Mesometeorology (CCRM, I. Zawadzki, president) at McGill University for the confidence put in us with the mandate of the MC2 development.

Within RPN and AES, we benefit strongly from the commitment of several people, particularly M. Béland, former head of Meteorological Research Branch, for his constantly positive management promotion; M. Valin, head of RPN programming section, for his unfailing advice on skillful coding strategies; and B. Bilodeau, research meteorologist, for his excellent support and frequent updates of the RPN physical processes code library.

We are also grateful to J. Abraham of the Maritime Weather Centre for initially suggesting and motivating us for the study on the suete winds. We also congratulate the MC2 user community for the wide spectrum of its model applications.

REFERENCES

Anthes, R. A., and T. T. Warner, 1978: Development of hydrodynamic models suitable for air pollution and other mesometeorological studies. *Mon. Wea. Rev.,* **106,** 1045–1078.

Asselin, R. A., 1972: Frequency filter for time integrations. *Mon. Wea. Rev.,* **100,** 487–490.

Bartello, P., O. Métais, and M. Lesieur, 1996: Geostrophic versus wave eddy viscosities in atmospheric models. *J. Atmos. Sci.,* **53,** 564–571.

Benoit, R., J. Côté, and J. Mailhot, 1989: Inclusion of a TKE boundary layer parameterization in the Canadian regional finite-element model. *Mon. Wea. Rev.,* **117,** 1726–1750.

——, S. Pellerin, and W. Yu, 1995: MC2 model performances during the Beaufort and Arctic Storms Experiment. *Atmos.–Ocean,* **35,** 221–244.

Bubnova, R., G. Hello, P. Bénard, and J.-F. Geleyn, 1995: Integration of the fully elastic equations cast in the hydrostatic pressure terrain-following coordinate in the framework of the ARPEGE/Aladin NWP system. *Mon. Wea. Rev.,* **123,** 515–535.

Burk, S. D., and W. T. Thompson, 1989: A vertically nested regional numerical weather prediction model with second-order closure physics. *Mon. Wea. Rev.,* **117,** 2305–2324.

Caya, D., R. Laprise, M. Giguère, G. Bergeron, J.-P. Blanchet, B. J. Stocks, G. J. Boer, and N. A. McFarlane, 1995: Description of the Canadian RCM. *Water Air Soil Pollut.,* **82** (1/2), 477–482.

Chouinard, C., J. Mailhot, H. L. Mitchell, A. Staniforth, and R. Hogue, 1994: The Canadian regional data assimilation system: Operational and research applications. *Mon. Wea. Rev.,* **122,** 1306–1325.

Clark, T. L., and W. R. Peltier, 1977: On the evolution and stability of finite-amplitude mountain waves. *J. Atmos. Sci.,* **34,** 1715–1730.

Côté, J., M. Roch, A. Staniforth, and L. Fillion, 1993: A variable-resolution semi-Lagrangian finite-element global model of the shallow-water equations. *Mon. Wea. Rev.,* **121,** 231–243.

——, S. Gravel, A. Méthot, A. Patoine, M. Roch, and A. Staniforth, 1995: Preliminary results from a dry global variable-resolution PE model. *Atmos.–Ocean,* **35,** 245–259.

Courtier, P., J. N. Thépaut, and A. Hollingsworth, 1994: A strategy for the operational implementation of 4D-var using an incremental approach. *Quart. J. Roy. Meteor. Soc.,* **120,** 1367–1387.

Daley, R. W., 1988: The normal modes of the spherical non-hydrostatic equations with applications to the filtering of acoustic modes. *Tellus,* **40A,** 96–106.

Davies, H. C., 1976: A lateral boundary formulation for multi-level prediction models. *Quart. J. Roy. Meteor. Soc.,* **102,** 405–418.

Deardorff, J. W., 1978: Efficient prediction of ground surface temperature and moisture with inclusion of a layer of vegetation. *J. Geophys. Res.,* **83,** 1889–1903.

Delage, Y., 1988: The position of the lowest levels in the boundary layer of atmospheric circulation models. *Atmos.–Ocean,* **26,** 329–340.

Dirks, R. A., J. P. Kuettner, and J. A. Moore, 1988: Genesis of Atlantic Lows Experiment (GALE): An overview. *Bull. Amer. Meteor. Soc.,* **69,** 148–160.

Durran, D. R., 1986: Another look at downslope windstorms. Part I: The development of analogs to supercritical flow in an infinitely deep, continuously stratified fluid. *J. Atmos. Sci.,* **43,** 2527–2543.

——, 1990: Mountain waves and downslope winds. *Atmospheric Processes over Complex Terrain,* W. Blumen, Ed., Amer. Meteor. Soc., 59–82.

Fouquart, Y., and B. Bonnel, 1980: Computations of solar heating of the earth's atmosphere: A new parameterization. *Contrib. Atmos. Phys.,* **53,** 35–62.

Fritsch, J. M., and C. F. Chappell, 1980: Numerical prediction of convectively driven mesoscale pressure systems. Part I: Convective parameterization. *J. Atmos. Sci.,* **37,** 1722–1733.

Gal-Chen, T., and R. Somerville, 1975: On the use of a coordinate transformation for the solution of the Navier–Stokes equations. *J. Comput. Phys.,* **17**(2), 209–228.

Garand, L., 1983: Some improvements and complements to the infrared emissivity algorithm including a parameterization of the absorption in the continuum region. *J. Atmos. Sci.,* **40,** 230–244.

——, and J. Mailhot, 1990: The influence of infrared radiation on numerical weather forecasts. Preprints, *Seventh Conf. on Atmospheric Radiation,* San Francisco, CA, Amer. Meteor. Soc., J146–J151.

Grell, G. A., J. Dudhia, and D. R. Stauffer, 1993: A description of the fifth-generation Penn State/NCAR mesoscale model (MM5). NCAR Tech. Note NCAR/TN-398, 122 pp. [Available from NCAR Information Services, P.O. Box 3000, Boulder, CO 80307.]

Gyakum, J. R., and Coauthors, 1995: First COMPARE workshop summary. *Bull. Amer. Meteor. Soc.,* **76,** 1209–1218.

——, and Coauthors, 1996: A regional model intercomparison using a case of explosive oceanic cyclogenesis. *Wea. Forecasting,* **11,** 521–543.

Héreil, P., and R. Laprise, 1996: Sensitivity of internal gravity waves solutions to the time step of a semi-implicit semi-Lagrangian nonhydrostatic model. *Mon. Wea. Rev.,* **124,** 972–999.

Holton, J. R., 1992: *An Introduction to Dynamic Meteorology.* 3d ed. Academic Press, 511 pp.

Hoskins, B. J., M. E. McIntyre, and A. W. Robertson, 1985: On the use and significance of isentropic potential vorticity maps. *Quart. J. Roy. Meteor. Soc.,* **111,** 877–946.

Imbard, M., R. Juvanon du Vachat, A. Joly, Y. Durand, A. Craplet, J.-F. Geleyn, J. M. Audoin, N. Marie, and J. M. Pairin, 1987: The Peridot fine-mesh numerical weather prediction system: Description, evaluation and experiments. *Short- and Medium-Range Numerical Weather Prediction,* T. Matsuno, Ed., Meteor. Soc. Japan, 455–465.

Jackson, P. L., and D. G. Steyn, 1994: Gap winds in a fjord. Part I: Observations and numerical simulation. *Mon. Wea. Rev.,* **122,** 2645–2665.

Jakimow, G., E. Yakimiw, and A. Robert, 1992: An implicit formulation for horizontal diffusion in gridpoint models. *Mon. Wea. Rev.,* **120,** 124–130.

Kain, J. S., and J. M. Fritsch, 1990: A one-dimensional entraining/detraining plume model and its application in convective parameterization. *J. Atmos. Sci.,* **47,** 2784–2802.

Klemp, J. B., and D. K. Lilly, 1975: The dynamics of wave-induced downslope winds. *J. Atmos. Sci.,* **32,** 320–339.

——, and R. B. Wilhelmson, 1978: Simulations of three-dimensional convective storm dynamics. *J. Atmos. Sci.,* **35,** 1070–1096.

Kuo, H. L., 1974: Further studies of the parameterization of the influence of cumulus convection on large-scale flow. *J. Atmos. Sci.,* **31,** 1232–1240.

Laprise, R., 1995: The formulation of André Robert's MC2 (Mesoscale Compressible Community) model. *Atmos.–Ocean,* **35,** 195–200.

——, and W. R. Peltier, 1989a: The linear stability of nonlinear mountain waves: Implications for the understanding of severe downslope windstorms. *J. Atmos. Sci.,* **46,** 545–564.

——, and ——, 1989b: On the structural characteristics of steady finite-amplitude mountain waves over bell-shaped topography. *J. Atmos. Sci.,* **46,** 586–595.

Long, R. R., 1953: Some aspect of the flow of stratified fluids. I: A theoretical investigation. *Tellus,* **5,** 42–58.

——, 1954: Some aspect of the flow of stratified fluids. II: Experiments with a two-fluid system. *Tellus,* **6,** 97–115.

Lott, F., and M. Miller, 1994: A new sub-grid scale orographic drag parametrization: Its formulation and testing. ECMWF Research Dept. Tech. Memo. 218, 59 pp. [Available from ECMWF, Reading, RG2 9AX, UK.]

Mailhot, J., 1994: The Regional Finite-Element (RFE) Model scientific description. Part 2: Physics. [Available from RPN, 2121 Trans-Canada, Dorval, QC H9P 1J3, Canada]

——, and C. Chouinard, 1989: Numerical forecasts of explosive winter storms: Sensitivity experiments with a meso-alpha-scale model. *Mon. Wea. Rev.,* **117,** 1311–1343.

——, ——, R. Benoit, M. Roch, G. Verner, J. Côté, and J. Pudykiewicz, 1989: Numerical forecasting of winter coastal storms during CASP: Evaluation of the regional finite-element model. *Atmos.–Ocean,* **27,** 27–58.

——, and Coauthors, 1995a: Changes to the Canadian regional forecast system: Description and evaluation of the 50-km version. *Atmos.–Ocean,* **33,** 55–80.

——, R. Benoit, P. Pellerin, V. Lee, N. Kouwen, E. D. Soulis, G. Kite, and L. Welsh, 1995b: Fine-scale modelling of intense orographic precipitation over the Columbia River Basin and coupling with distributed hydrology models. *Proc. Canadian Water Resources Association 48th Annual Conf.,* Fredericton, New Brunswick, Canada, CWRA, 589–604.

McFarlane, N. A., 1987: The effect of orographically excited gravity wave drag on the general circulation of the lower stratosphere and troposphere. *J. Atmos. Sci.,* **44,** 1775–1800.

Palko, S., L. St-Laurent, T. Huffman, and E. Unrau, 1996: The Canada vegetation and land cover: A raster and vector data set for GIS applications—Uses in agriculture. *GIS Applications in Natural Resources 2,* M. Heit et al., Eds., GIS World, 185–191.

Peaceman, D. W., and H. H. Rachford, 1955: The numerical solution of parabolic and elliptic differential equations. *SIAM,* **3** (1), 28–41.

Pellerin, P., R. Laprise, and I. Zawadzki, 1995: The performance of a semi-Lagrangian transport scheme for the advection–condensation problem. *Mon. Wea. Rev.,* **123,** 3318–3330.

Peltier, W. R., and T. L. Clark, 1979: The evolution and stability of finite-amplitude mountain waves. Part II: Surface wave drag and severe downslope windstorms. *J. Atmos. Sci.,* **36,** 1498–1529.

Pielke, R. A., and Coauthors, 1992: A comprehensive meteorological modeling system—RAMS. *Meteor. Atmos. Phys.,* **49,** 69–91.

Pierrehumbert, R. T., and B. Wyman, 1985: Upstream effects of mesoscale mountains. *J. Atmos. Sci.,* **42,** 977–1003.

Pinty, J.-P., R. Benoit, E. Richard, and R. Laprise, 1995: Simple tests of a semi-implicit semi-Lagrangian model on 2D mountain wave problems. *Mon. Wea. Rev.,* **123,** 3042–3058.

Queney, P., 1948: The problem of airflow over mountains. A summary of theoretical studies. *Bull. Amer. Meteor. Soc.,* **29,** 16–26.

Ritchie, H., 1991: Application of the semi-Lagrangian method to a multilevel spectral primitive-equations model. *Quart. J. Roy. Meteor. Soc.,* **117,** 91–106.

——, and M. Tanguay, 1996: A comparison of spatially averaged Eulerian and semi-Lagrangian treatments of mountains. *Mon. Wea. Rev.,* **124,** 167–181.

Robert, A., and E. Yakimiw, 1986: Identification and elimination of an inflow boundary computational solution in limited area model integrations. *Atmos.–Ocean,* **24,** 369–385.

Sass, B. H., and J. H. Christensen, 1995: A simple framework for testing the quality of atmospheric limited-area models. *Mon. Wea. Rev.,* **123,** 444–459.

Simmons, A. J., B. J. Hoskins, and D. M. Burridge, 1978: Stability of the semi-implicit method of time integration. *Mon. Wea. Rev.,* **106,** 405–412.

Smith, R. B., 1985: On severe downslope winds. *J. Atmos. Sci.,* **42,** 2597–2603.

Stein, J., 1992: Investigation of the regime diagram of hydrostatic flow over a mountain with a primitive equation model. Part I: Two-dimensional flows. *Mon. Wea. Rev.,* **120,** 2962–2976.

Stewart, R. E., R. W. Shaw, and G. A. Isaac, 1987: Canadian Atlantic Storms Program: The meteorological field project. *Bull. Amer. Meteor. Soc.,* **68,** 338–345.

Sundqvist, H., E. Berge, and J. E. Kristjansson, 1989: Condensation and cloud parameterization studies with a mesoscale numerical weather prediction model. *Mon. Wea. Rev.,* **117,** 1641–1657.

Tanguay, M., A. Robert, and R. Laprise, 1990: A semi-implicit semi-Lagrangian fully compressible regional forecast model. *Mon. Wea. Rev.,* **118,** 1970–1980.

——, E. Yakimiw, H. Ritchie, and A. Robert, 1992: Advantages of spatial averaging in semi-Lagrangian schemes. *Mon. Wea. Rev.,* **120,** 113–123.

Tapp, M. C., and P. W. White, 1976: A nonhydrostatic mesoscale model. *Quart. J. Roy. Meteor. Soc.,* **102,** 277–296.

Temperton, C., and M. Roch, 1991: Implicit normal mode initialization for an operational regional model. *Mon. Wea. Rev.,* **119,** 667–677.

Tokioka, T., 1978: Some considerations on vertical differencing. *J. Meteor. Soc. Japan,* **56,** 98–111.

Tremblay, A., A. Glazer, W. Yu, and R. Benoit, 1996: A mixed-phase cloud scheme based on a single prognostic equation. *Tellus,* **48A,** 483–500.

Verseghy, D. L., N. A. McFarlane, and M. Lazare, 1993: CLASS—A Canadian land surface scheme for GCMs. II. Vegetation model and coupled runs. *Int. J. Climatol.,* **13,** 347–370.

Yakimiw, E., and A. Robert, 1990: Validation experiments for a nested grid-point regional forecast model. *Atmos.–Ocean,* **28,** 466–472.

Zawadzki, I., L. Ostiguy, and R. Laprise, 1994: Retrieval of the microphysical properties in a CASP storm by integration of numerical kinematical model. *Atmos.–Ocean,* **31,** 201–233.